Holocene sea-ice dynamics in Petermann Fjord in relation to ice tongue stability and Nares Strait ice arch formation

Henrieka Detlef[1,2], Brendan Reilly[3], Anne Jennings[4], Mads Mørk Jensen[5], Matt O'Regan[6], Marianne Glasius[5], Jesper Olsen[2,7,8], Martin Jakobsson[6], Christof Pearce[1,2]

[1]Department of Geoscience, Aarhus University, Høegh-Guldbergs Gade 2, 8000 Aarhus C, Denmark
[2]Arctic Research Centre, Aarhus University, Ny Munkegade 114, 8000 Aarhus C, Denmark
[3]Scripps Institution of Oceanography, University of California San Diego, La Jolla, California, USA
[4]Institute of Arctic and Alpine Research, University of Colorado, Boulder, CO 80309-0450, USA
[5]Department of Chemistry, Aarhus University, Langelandsgade 140, 8000 Aarhus C, Denmark
[6]Department of Geological Sciences, Stockholm University, 106 91 Stockholm, Sweden
[7]Department of Physics and Astronomy, Aarhus University, Ny Munkegade 120, 8000 Aarhus C, Denmark
[8]School of Culture and Society – Centre for Urban Network Evolutions, Moesgård Alle 20, 8270 Højbjerg, Denmark

Correspondence to: Henrieka Detlef (henrieka.detlef@geo.au.dk)

Abstract. *The Petermann 2015 Expedition* to Petermann Fjord and adjacent Hall Basin recovered a transect of cores from Nares Strait to under the 48 km long ice tongue of Petermann glacier, offering a unique opportunity to study ice-ocean-sea ice interactions at the interface of these realms. First results suggest that no ice tongue existed in Petermann Fjord for large parts of the Holocene, raising the question of the role of the ocean and the marine cryosphere in the collapse and re-establishment of the ice tongue. Here we use a multi-proxy approach (sea-ice related biomarkers, total organic carbon and its carbon isotopic composition, and benthic and planktonic foraminiferal abundances) to explore Holocene sea-ice dynamics at OD1507-03TC-41GC-03PC in outer Petermann Fjord. Our results are in line with a tight coupling of the marine and terrestrial cryosphere in this region and, in connection with other regional sea-ice reconstructions, give insights into the Holocene evolution of ice arches and associated landfast ice in Nares Strait.

The late stages of the regional Holocene Thermal Maximum (6,900-5,500 cal yrs BP) were marked by reduced seasonal sea-ice concentrations in Nares Strait and the lack of ice arch formation. This was followed by a transitional period towards Neoglacial cooling from 5,500-3,500 cal yrs BP, where a southern ice arch might have formed, but an early seasonal break-up and late formation likely caused a prolonged open water season and enhanced pelagic productivity in Nares Strait. Between 3,500 cal yrs BP and 1,400 cal yrs BP, regional records suggest the formation of a stable northern ice arch only, with a short period from 2,500-2,100 cal yrs BP where a southern ice arch might have formed intermittently in response to atmospheric cooling spikes. A stable southern ice arch, or even double arching, is also inferred for the period after 1,400 cal yrs BP. Thus, both the inception of a small Petermann ice tongue at ~2,200 cal yrs BP and its rapid expansion at ~600 cal yrs BP are preceded by a transition towards a southern ice arch regime with landfast ice formation in Nares Strait, suggesting a stabilizing effect of landfast sea ice on Petermann Glacier.

1 Introduction

35   Nares Strait, connecting the Lincoln Sea to the northern Baffin Bay, is an important conduit for sea ice, freshwater and heat between the Arctic Ocean and the western North Atlantic. The annual flux of freshwater through Nares Strait, in liquid and solid form, heavily depends on the seasonal formation of ice arches (Kwok et al., 2010; Münchow, 2016; Rasmussen et al., 2010). Ice arches form when drift ice converges in a narrow passage between two landmasses. In Nares Strait their formation depends primarily on the sea-ice thickness, local wind stresses, and atmospheric temperatures (Barber et al., 2001; Kwok et

40   al., 2010; Samelson et al., 2006). Ice arching inhibits sea-ice export from the Arctic Ocean and allows the formation of landfast ice in Nares Strait, consisting of a mixture of multi-year drift ice, originating from the Arctic Ocean, and locally formed first-year ice (Kwok, 2005; Kwok et al., 2010). Historically, the formation of a northern and southern arch have been observed in Robeson Channel and Smith Sound, respectively (Fig. 1) (Vincent, 2019). In recent decades, however, changes in the ice arch configuration suggest a transition in Nares Strait sea-ice dynamics. Between 1979 and 2019, Nares Strait was blocked for sea-

45   ice passage on average 161 days per season with a consistent decrease of 2.1 days/year throughout this period (Vincent, 2019). This is also associated with an emerging prominence of the northern arch (Vincent, 2019). In the winter of 2006/2007 both ice arches failed to form for the first time in recorded history, causing sea ice to remain mobile in Nares Strait year-round (Kwok et al., 2010; Vincent, 2019) (Fig. 2, Supplementary Fig. 1). The observed changes in Nares Strait sea-ice dynamics likely have significant consequences for the export of multi-year sea ice from the Lincoln Sea and long-term Arctic sea-ice loss (Kwok et

50   al., 2010; Moore et al., 2021; Vincent, 2019) (Fig. 2). Additionally, the formation of the southern ice arch in Smith Sound is crucial for the annual opening of the North Water Polynya (NOW) (Fig. 1) and the formation of landfast sea ice in Nares Strait (Barber et al., 2001). The latter has important implications for the hydrographic structure in Nares Strait and its adjacent fjords in response to changing wind stresses on surface waters in Nares Strait (Shroyer et al., 2015, 2017).

The water column in Nares Strait is characterized by cold and fresh Polar Water (PW) in the upper 50-100 m with warmer and

55   more saline modified/Arctic Atlantic Water (AAW) below, separated by a strong halocline (Johnson et al., 2011; Münchow et al., 2014). Under landfast sea ice, Ekman transport causes eastward displacement of cold and fresh PW towards the Greenland coast (Rabe et al., 2012; Shroyer et al., 2015, 2017). Conversely, mobile sea ice leads to westward Ekman transport of PW and upwelling of AAW in the east, increasing the oceanic heat flux to fjord systems along the Greenland coast of Nares Strait (Münchow et al., 2007; Shroyer et al., 2017). Outlet glaciers draining into fjords in the north and northeast of Greenland, commonly terminate in a floating ice tongue of variable length, with three glaciers terminating in an ice tongue >10 km (Hill

60   et al., 2017). One such glacier is Petermann Glacier (PG), draining about 4 % of the Greenland Ice Sheet (GrIS) (based on area of the drainage basin (Rignot and Kanagaratnam, 2006)) into Hall Basin in Nares Strait (Fig. 1). Large calving events of PGs floating ice tongue in 2010 and 2012 (Johannessen et al., 2013; Rückamp et al., 2019) were associated with a 10 % acceleration of the glacier (Rückamp et al., 2019). Interestingly, the 2010 calving event occurred at the end of a 4-year period with no/little

65   landfast ice in Nares Strait and associated earlier break-up of landfast ice in Petermann Fjord (Fig. 2). The smaller calving

event in 2012, on the other hand, followed the re-establishment of extensive landfast ice in Nares Strait in 2011 (Fig. 2). Although the calving events have attracted considerable attention, submarine melting of the ice tongue accounts for 80 % of the mass loss at PG, making it particularly sensitive to ice-ocean interactions (Cai et al., 2017; Münchow et al., 2014; Rignot and Steffen, 2008; Rückamp et al., 2019).

70
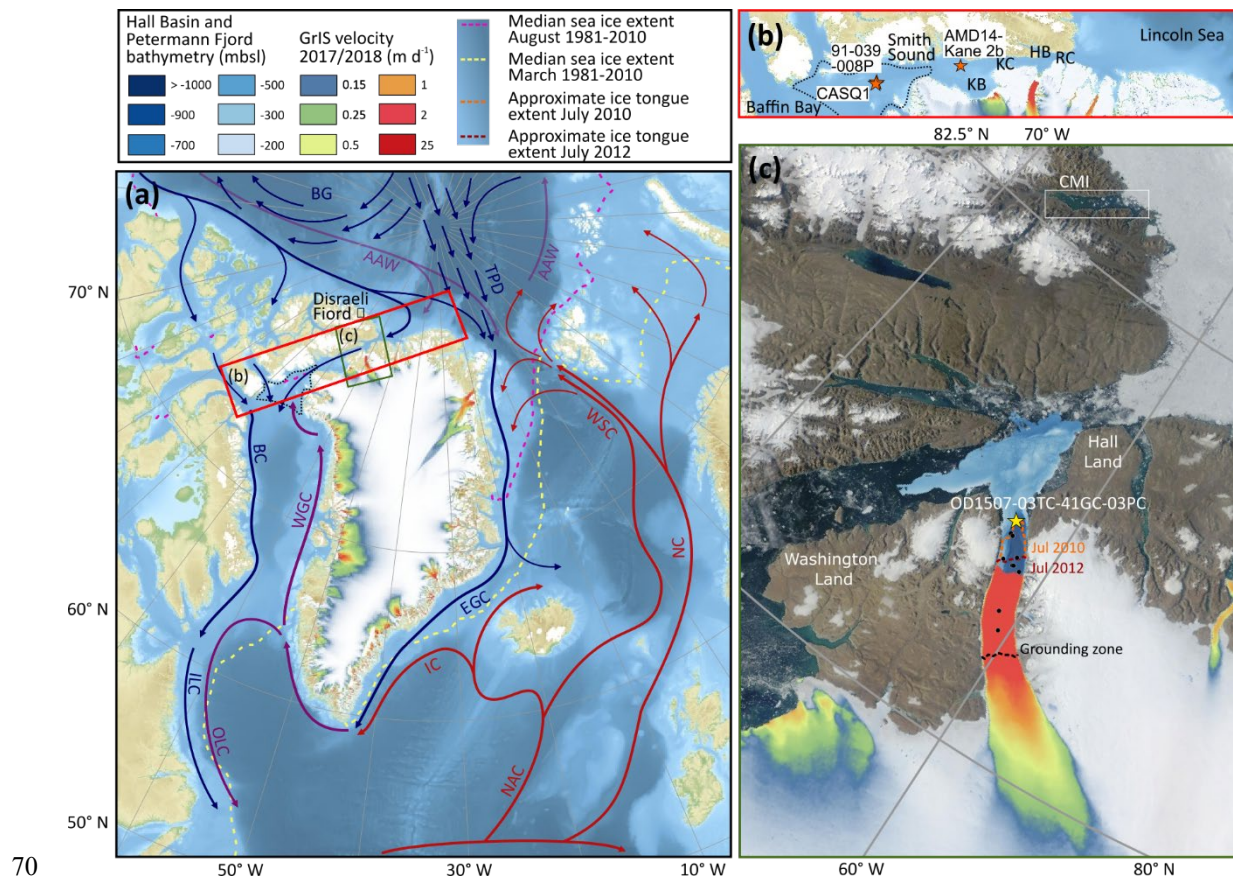
Figure 1. Map of the study area. (a) Map of the North Atlantic, including major surface currents (AAW: Arctic Atlantic Water, BC: Baffin Current, BG: Beaufort Gyre, EGC: East Greenland Current, IC: Irminger Current, ILC: Inner Labrador Current, NAC: North Atlantic Current, NC: Norwegian Current, OLC: Outer Labrador Current, TPD: Trans Polar Drift, WGC: West Greenland Current, WSC: West Spitsbergen Current), median August (dashed, pink) and March (dashed, yellow) sea ice extent from 1981-
75   2010 (Fetterer et al., 2017), the velocity of the Greenland Ice Sheet (GrIS) 2016/2017 (Nagler et al., 2015), and the location of Disraeli Fiord (Ellesmere Island). The approximate extent of the NOW polynya (mean extent in May 1954-1968) (Dunbar, 1969) is indicated with a black dashed line. (b) Close-up of Nares Strait, connecting Lincoln Sea to northern Baffin Bay, consisting of Robeson Channel (RC), Hall Basin (HB), Kennedy Channel (KC), Kane Basin (KB), and Smith Sound. The red stars indicate additional sediment cores discussed in this manuscript. These are AMD14-Kane2b (Kane Basin; Georgiadis et al. (2020)), QASQ1 (central NOW;
80   Jackson et al. (2021)), and 91-039-008P (central NOW; Knudsen et al. (2008)). (c) Close up of the Petermann Fjord and Petermann glacier (satellite image from 'NASA Worldview' (https://worldview.earthdata.nasa.gov/)) including the location of Clements Markham Inlet (CMI), the Hall Basin and Petermann Fjord bathymetry (Jakobsson et al., 2018), the velocity of the Greenland Ice Sheet (GrIS) 2016/2017 (Nagler et al., 2015), the grounding zone location of Petermann glacier (black, dashed), and the ice tongue extent in July 2010 (orange, dashed) and 2012 (red, dashed). The core location of OD1507-03TC-41GC-03PC is indicated with a
85   yellow star, the black dots show additional core sites from *The Petermann 2015 Expedition* used in Reilly et al. (2019) to reconstruct the Holocene extent of the PG ice tongue.

Submarine melt rates depend on the turbulent heat flux reaching the ice tongue/ocean interface. This is a function of the oceanic heat content, determined by the inflow of AAW to Petermann Fjord, and turbulent mixing underneath the ice tongue, promoted by subglacial meltwater discharge (Cai et al., 2017; Washam et al., 2018). Thus, changes in Nares Strait sea-ice dynamics, that modify AAW inflow to Petermann Fjord, may affect the ice tongue stability on long timescales. Additionally, earlier work has identified landfast sea ice in fjords around Greenland as an important mechanism stabilizing the calving front of marine-terminating outlet glaciers, with the loss of landfast ice prolonging the calving season (Amundson et al., 2010; Carr et al., 2015; Robel, 2017; Todd and Christoffersen, 2014). Hence, in light of the recent doubling of mass loss from the GrIS (Shepherd et al., 2012) a detailed understanding of ocean-sea ice-glacier interactions on longer timescales is essential to improve projections for the contribution of the GrIS to future sea level rise (Fürst et al., 2015; Stocker et al., 2013).

In 2015, the Swedish Icebreaker *Oden* set out for *The Petermann 2015 Expedition* to improve our understanding of the processes involved in ocean-sea ice-glacier interactions and the sensitivity of PGs floating ice tongue to Holocene climate change. A transect of sediment cores, extending from Hall Basin to underneath the Petermann ice tongue, was recovered (Reilly et al., 2019). Spatial differences in sediment facies associated with the presence/absence of the ice tongue allowed the reconstruction of the extent of the Petermann ice tongue over the last ~7,000 cal yrs BP (Reilly et al., 2019). Reilly et al. (2019) demonstrate that after the deglacial break-up of the ice tongue at ~6,900 cal yrs BP, no stable ice tongue existed in Petermann Fjord for the largest part of the mid-Holocene, with a small ice tongue re-emerging at ~2,200 cal yrs BP, which advanced to its modern limits around 600 years ago.

Here, we focus on the Holocene evolution of sea-ice conditions in Petermann Fjord. The spliced sediment core OD1507-03TC-41GC-03PC (81.192° N; -62.023° E; 976 m water depth) located in outer Petermann Fjord (Fig. 1), offers a unique opportunity to study Nares Strait and local sea-ice dynamics, and their influence on the stability of PG. Sea-ice reconstructions are based on source-specific Arctic sea-ice biomarkers (Belt, 2018). Measurements of total organic carbon (TOC), the carbon isotopic composition of TOC, sterol biomarkers and the benthic and planktonic foraminiferal abundance provide information with regard to marine primary productivity and terrestrial organic carbon input to Petermann Fjord across the Holocene. In combination with existing studies (e.g. England et al., 2008; Funder et al., 2011; Georgiadis et al., 2020) our results offer insights into the Holocene development of ice arches in Nares Strait. Importantly, this study demonstrates that the development of more severe sea-ice conditions in Petermann Fjord preceded major advances of the ice tongue, indicating a stabilizing effect on PG.

2. Regional oceanography

At the northern end of Nares Strait, Robeson Channel connects Hall Basin to the Lincoln Sea (Fig. 1) with water mass exchange controlled by a 290 m deep sill (Münchow et al., 2011a; Washam et al., 2018). In the upper 50 m (off Greenland) to 100 m (off Ellesmere Island) (Jones and Eert, 2004; Münchow et al., 2007), Nares Strait is characterized by relatively fresh and nutrient-rich Polar Water (PW). Geochemical tracers suggest that these waters are primarily of North Pacific origin, entering

the Arctic Ocean via the Bering Strait, modified by river runoff and sea-ice melt (Jones and Eert, 2004; Münchow et al., 2007).

120 Below (>300 m in Hall Basin), the water column is characterized by AAW (0.28-0.31 °C; (Washam et al., 2018)) (Jones and Eert, 2004). Hydrographic surveys have shown that the AAW in Nares Strait has warmed by 0.023 ± 0.015 °C per year between 2003 and 2009 (Münchow et al., 2011b). At its shallowest, at the northern end of Kane Basin, Nares Strait is 220 m deep (Münchow and Melling, 2008). This sill impedes the southward flow of AAW, suggesting that Atlantic Water at the southern end of Nares Strait is predominantly derived from the north flowing West Greenland Current (Fig. 1) (Melling et al., 2001).

125 The circulation in Nares Strait is dominated by a southward surface jet controlled by winds and along channel pressure gradients between the Lincoln Sea and northern Baffin Bay (Rabe et al., 2010, 2012). The hydrographic structure in Nares Strait varies according to the predominant sea-ice state (Rabe et al., 2012; Shroyer et al., 2015, 2017). Modelling studies show that this is a response to surface stresses (Shroyer et al., 2015, 2017). Landfast sea ice exerts a northward drag at the ocean surface, resulting in eastward Ekman transport of cool and fresh PW and a westward shift of the main surface jet towards

130 Ellesmere Island (Rabe et al., 2012; Shroyer et al., 2015, 2017). During the mobile sea-ice season southward wind stress and associated westward Ekman surface transport cause a displacement of cool and fresh surface waters towards Ellesmere Island and upwelling of relatively warm and salty waters along the Greenland coast, while the main southward flow is concentrated in the centre of the channel (Münchow et al., 2007; Shroyer et al., 2017). Nares Strait is covered by sea ice for around 10-11 months per year, with a 95% ice cover during winter months (Rasmussen et al., 2010). Summer break-up occurs in June/July,

135 with renewed freeze up in late September/October. The flow of sea ice through Nares Strait is highest during fall and early winter (Kwok et al., 2010) with large interannual variability depending on the formation and duration of the northern and southern ice arch. While the formation of either arch will block the export of Arctic sea ice through Nares Strait, only the formation of the southern arch leads to the opening of the NOW (Barber et al., 2001) and a complete freeze up of Nares Strait (Kwok, 2005; Kwok et al., 2010).

140 Petermann Fjord, connected to Nares Strait (Hall Basin) via a 350-450 m deep sill, is up to 1100 m deep and ~20 km wide (Jakobsson et al., 2018). It hosts a floating ice tongue, approximately 48 km long (from the grounding zone) with an average width of 16.6 km and a thickness of 600 m at the grounding zone to 200 m at the terminus (Heuzé et al., 2017; Johannessen et al., 2013). The ice tongue flows at a speed of 1250 ± 90 m yr^{-1} over the grounding zone, resulting in a calculated net glacial freshwater flux of 0.26 mSv (Heuzé et al., 2017). The formation of landfast ice in Petermann Fjord is somewhat independent

145 of the formation of landfast ice in Nares Strait. Landfast ice in Petermann Fjord will also form when sea ice in Nares Strait remains mobile throughout the winter (e.g. 2007, 2009, 2010; Fig. 2), although the sea-ice state in Nares Strait likely influences the timing of sea-ice break-up in Petermann Fjord in spring/summer, with earlier/later break-up during years without/with landfast sea ice in Nares Strait (Fig. 2, Supplementary Fig. 1). Additionally, we propose that the sea-ice dynamics in Nares Strait likely have important implications for the primary productivity regime in Petermann Fjord, with ice edge conditions in

150 spring/ early summer in years with mobile sea ice in Nares Strait (e.g. 2007 and 2009; Supplementary Fig. 1), while under landfast ice conditions in Nares Strait the spring/early summer ice edge is situated several hundred kilometres to the southwest in Kane Basin/Smith Sound (e.g. 2013 and 2014; Supplementary Fig. 1). Since the spring ice edge is a highly productive

system, especially important for the sympagic algal bloom (Ardyna and Arrigo, 2020; Leu et al., 2015; Wassmann and Reigstad, 2011), the position of the Nares Strait ice edge is likely to play a role for the local primary productivity.
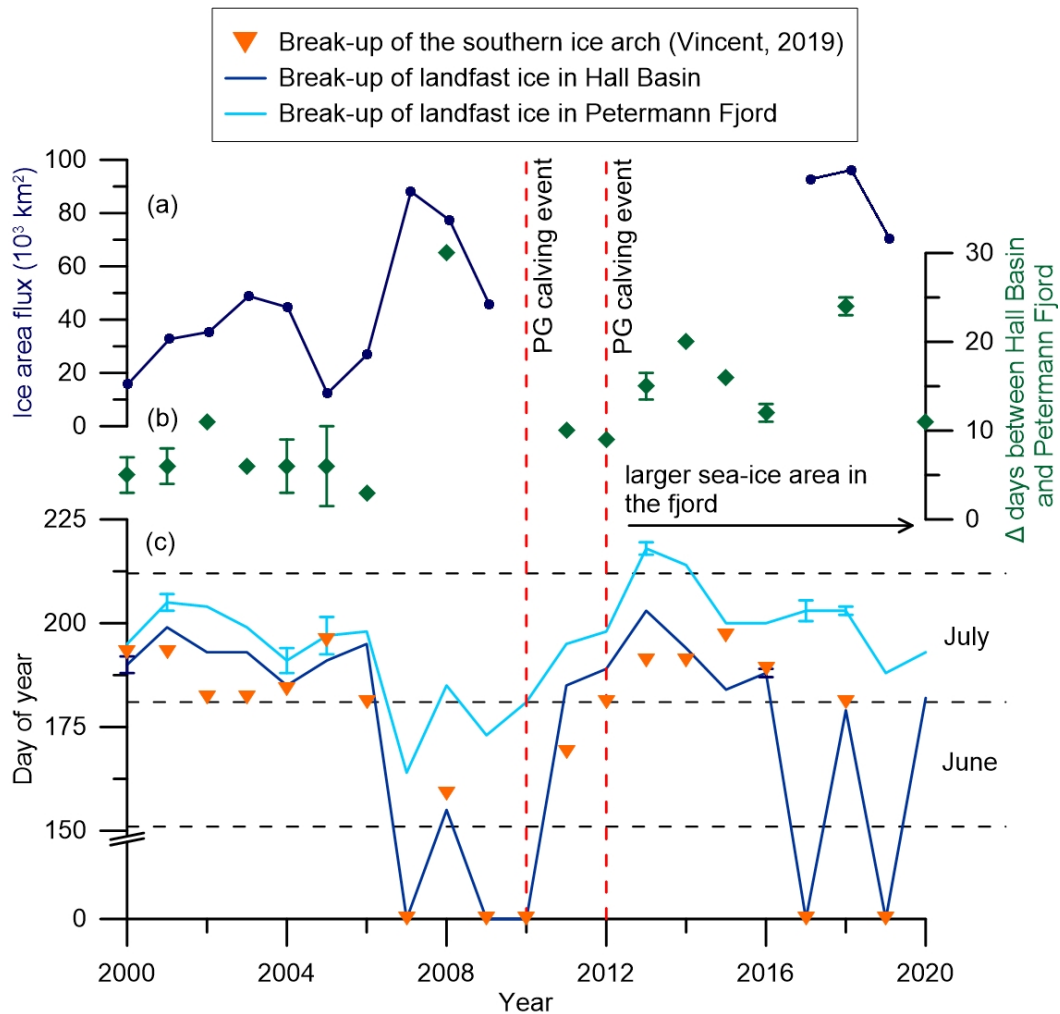
Figure 2. Modern ice arch dynamics in Nares Strait. (a) Annual mean ice area flux through southern Lincoln Sea flux gate (2000-2009 (Kwok et al., 2010), 2017-2019 (Moore et al., 2021)). (b) Difference between ice break-up in Hall Basin and Petermann Fjord in days. After 2010/2012 the differences increase due to the larger sea-ice area in Petermann Fjord following the retreat of the ice tongue. (c) Time series of approximate landfast sea-ice break-up in Petermann Fjord (light blue) and Hall Basin (dark blue) from 2000-2020 estimated from https://worldview.earthdata.nasa.gov/. The orange triangles represent the day of year when the southern ice arch collapsed (Vincent, 2019). Where the Hall Basin and ice arch break-up record have a day of year of zero, landfast sea ice did not form in Nares Strait throughout the entire year. Where cloud cover inhibited the exact determination of the day of landfast sea-ice break-up, the average between the last clear day with landfast ice and the first clear day following ice break-up was used (Hall Basin: 2000,2016; Petermann Fjord: 2001, 2004, 2005, 2013, 2017, 2018). Error bars indicate the timespan where cloud cover inhibited clear determination of the sea-ice state. The dashed vertical lines indicate years of substantial ice tongue calving in Petermann Fjord.

The hydrographic structure in Petermann Fjord is closely linked to that in Nares Strait with colder, fresher PW overlaying AAW (Johnson et al., 2011; Münchow et al., 2014). Bottom waters in Petermann Fjord are renewed by episodic spillover of

AAW from Hall Basin, with bottom water properties in Petermann Fjord resembling those at ~380 m water depth in Hall Basin
170   (effective sill depth) (Johnson et al., 2011). In general, the circulation in Petermann Fjord resembles an estuarine model, with outflow of buoyant, meltwater-enriched surface waters along the northeast side of the fjord and inflow of AAW below, concentrated along the south-western side of the fjord mouth (Heuzé et al., 2017; Johnson et al., 2011; Washam et al., 2018). In the fjord mouth, eddy structures can enhance the exchange between Hall Basin and Petermann Fjord. Eddies are stronger and more stable during summer, when sea ice in Nares Strait is mobile (Johnson et al., 2011; Shroyer et al., 2017). Modelling
175   studies suggest that the displacement of water masses in Nares Strait in response to the prevailing sea-ice regime also affects Petermann Fjord, with enhanced inflow of warmer, saltier AAW during times of mobile sea-ice (Shroyer et al., 2017). Additionally, a stronger circulation in the fjord, driven by enhanced subglacial runoff during summer months, increases the transport of AAW to the ice tongue cavity and the turbulent mixing of AAW toward the base of the ice tongue (Cai et al., 2017; Washam et al., 2018). In response to warming of AAW in Nares Strait (Münchow et al., 2011b), a 0.2°C warming of
180   AAW in Petermann Fjord has been observed from 2002 to 2016 (Washam et al., 2018). In combination, the greater oceanic heat flux and strengthened under ice currents cause enhanced submarine melting and non-steady state thinning of the ice tongue (Cai et al., 2017; Washam et al., 2018, 2019).

3. Materials and methods

3.1 Sediment core OD1507-03TC-41GC-03PC

185   Sediment core OD1507-03TC-41GC-03PC is stored at the Oregon State University Marine and Geology Repository at 2.8°C. Samples were taken approximately every 5 cm for the analysis of different organic constituents and approximately every 10 cm for benthic and planktonic foraminiferal analyses. The core represents a spliced record of a trigger core (TC), a gravity core (GC), and a piston core (PC) recovered in outer Petermann Fjord as part of *The Petermann 2015 Expedition* (Fig. 1) (Table 1). The splice has a total length of 556 cm and was recovered 80 km from the 2015 PG grounding zone at an average
190   water depth of 976 m (Reilly et al., 2019). Based on Computed Tomography (CT) scans, continuous sections with minimal disturbance were chosen for the splice and correlation was performed using X-Ray Fluorescence (XRF) Ti/Ca ratios, CT slice images, and CT numbers (Reilly et al., 2019) (Supplementary Table 1). Three sedimentary units are distinguished in OD1506-03TC-41GC-03PC, based on physical properties and XRF elemental data (Reilly et al., 2019). Sedimentary unit 3 (ca. 518-555 cm) is a massive diamict composed of a sandy mud with abundant coarse clasts and XRF Ti/Ca ratios around 0.05 (Reilly
195   et al., 2019). The clasts found in this unit, likely do not represent ice rafted debris (IRD), but instead are related to proximity of the grounding zone (Reilly et al., 2019). Unit 2, a clayey laminated mud with no or very low concentrations of coarser material (IRD), is found between ca. 398-518 cm (Reilly et al., 2019). The topmost lithofacies, unit 1 (0-398 cm), is a bioturbated clayey mud with isolated sand and coarser particles (Reilly et al., 2019). Based on the XRF Ti/Ca ratios and the abundance of coarse material, unit 1 has been divided into three subsections (A (0-53 cm), B (53-164 cm), C (164-398 cm))

(Reilly et al., 2019). Subunit 1C is marked by a decreasing trend from high to intermediate IRD occurrence, with intermediate IRD abundances continuing during subunit 1B, followed by low IRD abundance during subunit 1A (Reilly et al., 2019).

The age model for OD1507-03TC-41GC-03PC, established by Reilly et al. (2019), is based on radiocarbon (^{14}C) dating of benthic and planktonic foraminifera and calibration of radiocarbon ages using the Marine13 curve (Reimer et al., 2013) and MatCal MATLAB tools (Lougheed and Obrochta, 2016). The ΔR value was constrained using Paleosecular Variation (PSV) stratigraphy, with the best fit determined for a constant ΔR choice of 770 years (Reilly et al., 2019). No ages were determined for the interval between 408 cm and 556 cm, due to lack of radiocarbon dates. Regional constraints, however, suggest that these sediments are younger than 7,600 years, corresponding to the timing of the retreat of PG into the fjord (Jakobsson et al., 2018).

Table 1. Metadata of sediment cores used in the OD1507-03TC-41GC-03PC splice (Reilly et al. 2019).

Expedition	Deployment #	Core type	Latitude (°)	Longitude (°)	Water depth (m)	Length (cm)
OD1507	03	PC/TC	81.190	-62.068	960	606/95.3
OD1507	41	GC	81.194	-61.977	991	440

3.2 Sea-ice biomarker methodology

Reconstructions of past sea-ice conditions in Petermann Fjord rely on the identification of source-specific Arctic sea-ice biomarkers, together with the identification of common sterol biomarkers, TOC, and planktonic and benthic foraminiferal abundances. This is a qualitative method to determine past sea-ice dynamics. For clarity, we will describe past sea-ice conditions using the following categories in order of increasing average sea-ice concentration: ice free, reduced seasonal sea ice, enhanced seasonal sea ice, and near-perennial.

Source-specific sea-ice biomarkers include a mono- and a di-unsaturated highly branched isoprenoid (HBI), termed IP$_{25}$ (ice proxy with 25 carbon atoms) and HBI II (Belt, 2018; Belt et al., 2007). IP$_{25}$ is produced by a number of spring sea-ice dwelling diatoms, including *Haslea spicula*, *H. kjellmanii*, and *Pleurosigma stuxbergii* var. *rhomboides* (Brown et al., 2014). Thus, its presence in Arctic marine sediments provides evidence for past seasonal sea-ice occurrence, while the absence of IP$_{25}$ occurs in year-round ice-free environments as well as under perennial sea-ice cover (Belt, 2018; Belt et al., 2007; Brown et al., 2014; Navarro-Rodriguez et al., 2013; Xiao et al., 2015). Salinity changes might exert an additional control on IP$_{25}$ production, with Ribeiro et al. (2017), showing that its production appears to be suppressed by meltwater in fjords of North Eastern Greenland. Given its co-production in *H. spicula*, *H. kjellmanii*, and *Pleurosigma stuxbergii* var. *rhomboides* (Brown et al., 2014), HBI II co-varies with IP$_{25}$ in the Arctic realm. Thus, the typically higher HBI II concentrations can provide additional information during times of low/absent sedimentary IP$_{25}$.

In recent years, biomarker-based reconstructions of past sea-ice dynamics have commonly also reported a tri-unsaturated HBI (HBI III), produced by diatoms characteristic of the spring sea-ice edge bloom in the marginal ice zone (MIZ) (Belt et al., 2015, 2017; Smik et al., 2016). In Petermann Fjord, however, the identification of the HBI III peak in gas chromatography-

mass spectrometry (GC-MS) chromatograms was compromised due to interference with a neighbouring peak (Supplementary
Fig. 2). This is specific to sediment samples from Petermann Fjord, as HBI III could be identified in reference sediment from
Young Sound extracted alongside the samples from Petermann Fjord (see 3.3.2). Instead, we use a range of sterol biomarkers
(campesterol, cholesterol, brassicasterol, dinosterol, and β-sitosterol) and the abundance of benthic and planktonic foraminifera
to gain insights into the regional primary productivity regime and the addition of terrestrial organic carbon to Petermann Fjord.
Sterols are common compounds in eukaryotic cell membranes, abundant in both marine and terrestrial organic carbon. This
complicates their use as unambiguous tracers of a specific organism and/or environmental regime (Belt and Müller, 2013;
Rontani et al., 2014; Volkman, 1986). Nonetheless, the relative abundance of certain sterols can vary according to the
predominant organic carbon source (Rontani et al., 2014; Volkman, 1986; Yunker et al., 1995) (Table 2).

Table 2. Overview of the dominant sources of different sterol biomarkers measured in this study.

Biomarker	Predominant source organisms	References
Cholesterol	- In the marine realm: zoo- and phytoplankton - Also occurs in terrestrially derived organic carbon	Meyers and Ishiwatari (1993), Volkman (1986), Volkman (2003), Volkman et al. (2000), Yunker et al. (1995)
Brassicasterol	- Often the most abundant sterol in marine diatoms - In lower relative concentrations found in freshwater algae	Volkman (1986), Volkman (2003), Volkman et al. (2000), Yunker et al. (1995)
Dinosterol	- Major sterol in most dinoflagellate species - Also found in other marine microalgae (e.g. diatoms)	Belicka et al. (2004), Volkman (2003), Volkman et al. (2000)
Campesterol	- Dominant sterol in vascular plants - In minor amounts synthesized by marine microorganisms	Rontani et al. (2014), Volkman (1986), Yunker et al. (1995)
β-sitosterol	- Dominant sterol in vascular plants - In minor amounts synthesized by marine microorganisms	Rontani et al. (2014), Volkman (1986), Yunker et al. (1995)

Depending on the predominant primary producers, high concentrations of brassicasterol and dinosterol are reported from ice-
free regions, the MIZ, and under varying concentrations of seasonal sea ice (Xiao et al., 2015). In general sterol concentrations
are low under perennial sea ice in the Arctic Ocean, where all primary productivity is impeded due to limited light availability
(Xiao et al., 2015).

Here we use brassicasterol, dinosterol, and cholesterol to represent phytoplankton primary productivity in Petermann Fjord,
with different relative concentrations, potentially indicating changes in the ecosystem composition. Campesterol and β-
sitosterol, on the other hand, are used to gain insight into terrestrial organic carbon input. The multiproxy study of IP$_{25}$, HBI

II, sterol biomarkers, and the benthic and planktonic foraminiferal abundance (see section 3.4), thus allows interpretations of past sea-ice dynamics and terrestrial versus marine organic carbon input to Petermann Fjord.

3.3 Analysis of total organic carbon (TOC), carbon isotopic composition of TOC ($\delta^{13}C_{org}$), and sea-ice related biomarkers in sediments from OD1507-03TC-41GC-03PC

Prior to the analysis of organic constituents the samples were freeze-dried (-45 °C; 0.2 mbar; 48 h) at Aarhus University using a Christ Alpha 1-4 LSC freeze drier. The dried samples were weighed and dry bulk densities (DBD) were determined from the samples respective volume and dry weight. Subsequently, the samples were homogenized with a dichloromethane (DCM) cleaned pestle and mortar.

3.3.1 Total organic carbon (TOC) quantification and analysis of carbon isotopic composition of TOC ($\delta^{13}C_{org}$)

For TOC and $\delta^{13}C_{org}$, 10 mg of homogenized sample material was weighed into an Ag capsule (Elemental Microanalysis). Depending on available material, duplicates or triplicates were prepared to test for reproducibility. Additionally, a soil standard (10 mg; Elemental Microanalysis Soil Standard (Sandy) OAS 133506; 0.76 % *w/w* TOC) and blanks were added every ~15 samples. To remove the inorganic carbon, 35% HCl was added one drop at a time until no further reaction was observed (approximately 4 drops per sample, standard, and blank). The samples were then dried on a hotplate (50°C) overnight. The Ag capsules were folded and placed inside a Sn capsule (Elemental Microanalysis), which was packed tightly and stored in a desiccator until analysis.

The $\delta^{13}C_{org}$ and % wt TOC were measured using a continuous-flow IsoPrime IRMS coupled to an Elementar PyroCube elemental analyser at the Aarhus AMS Centre (AARAMS), Aarhus University, Denmark. $\delta^{13}C_{org}$ is reported in ‰ versus Vienna Pee Dee Belemnite (VPDB). An in-house standard Gel-A was used as primary standard yielding ±0.2‰ and ±0.3‰ for carbon and nitrogen analysis respectively. Further, secondary in-house and international standards were used to check the normalization to the VPDB. The mean reproducibility using 10 duplicate samples is ±0.03% and ±0.4‰ for % wt TOC and $\delta^{13}C_{org}$ respectively. For both acid pre-treated and non-acid pre-treated Elemental Microanalysis Soil Standard (Sandy) OAS 133506 samples the reproducibility of 7 samples is ±0.02% wt TOC. The $\delta^{13}C_{org}$ reproducibility of non-acid pre-treated Elemental Microanalysis Soil Standard (Sandy) OAS 133506 samples is ±0.1‰ whereas acid pre-treated samples show a mean reproducibility of ±0.5‰. TOC concentrations are reported in weight % (wt.%) and TOC fluxes ($\mu g\ cm^{-2}\ yr^{-1}$) are derived using the samples individual DBD and linear sedimentation rates (LSR), which were calculated using the datums from ^{14}C analysis of benthic and planktonic foraminifera (Reilly et al., 2019).

3.3.2 Lipid biomarker extraction and analysis

Biomarkers were extracted from 6.00±0.03 g freeze-dried sediment. A procedural blank and a reference sediment sample (~3 g) with known biomarker concentrations were added to each extraction batch (n = 12). 9-octylheptadec-8-ene (9-OHD) and 5α-androst-16-en-3α-ol (0.1 μg) were added to each sample, reference sediment, and blank, as internal standards for HBI and

sterol quantification, respectively. The samples were extracted using saponification (5% potassium hydroxide (KOH) in methanol (MeOH):H_2O (9:1, *v/v*); 70°C, 1 h) followed by extraction of the non-saponifiable lipids into hexane (3 x 2 mL).

280 According to polarity, the different lipid classes were separated using silica column chromatography. Nonpolar lipids, such as IP_{25} and HBI II were eluted with hexane, while the more polar sterols were eluted with DCM:MeOH (1:1, *v/v*) (~7 mL, each). Hexane fractions were further purified using silver nitrate silica column chromatography ($AgNO_3$ on SiO_2, ~10 wt.% of labelling), where the saturated hydrocarbons were eluted with hexane (2 mL) and the unsaturated compounds, including the HBIs, were eluted with acetone (7 mL), dried (N_2; 25°C) and transferred to GC-MS vials fitted with 300 µL inserts. The sterol

285 fractions were derivatised using N,O- Bis(trimethylsilyl)trifluoroacetamide (50 µL, 70 °C, 1 h) and transferred to 1.5 mL GC-MS vials.

All biomarker samples were analysed at Aarhus University using an Agilent 7890B GC fitted with an HP-5ms Ultra Inert column (30 m x 250 µm x 0.25 µm) coupled to a 5977A series mass selective detector and equipped with a Gerstel multipurpose sampler (MPS). Prior to analysis HBI and sterol extracts were diluted with 50 µL hexane (using the MPS system) and 0.500

290 mL DCM (manually), respectively. For GC-MS operating conditions see Supplementary Table 2. Following Belt (2018) the identification of individual lipids is based on their characteristic retention indices and mass spectra. Quantification is achieved by comparing the integrated peak area (PA) of the selected ion for each biomarker (Supplementary Table 2) to the PA of the respective internal standard (Belt et al., 2012) under consideration of an instrumental response factor (based on the reference sediment) and the mass or the TOC concentrations of the sediment extracted (Belt et al., 2012). Due to unknown concentrations

295 of dinosterol in the reference sediment, an individual response factor could not be determined for this compound. Instead, the average response factor for brassicasterol and cholesterol was used. Thus, while the relative dinosterol concentrations and trends hold true, absolute concentrations might not be accurate. In addition to the biomarker concentrations in ng g^{-1} of dry sediment (ng g^{-1} sed) and µg g^{-1} TOC, biomarker fluxes were calculated using the samples individual DBD and linear sedimentation rates (LSR). Fluxes are reported in ng cm^{-2} yr^{-1} and are interpreted alongside biomarker concentrations to avoid

300 bias related to jumps in the LSR.

3.4 Planktonic and benthic foraminiferal abundances

The OD1507-03TC-41GC-03PC benthic and planktonic foraminiferal abundances were determined on 58 samples. The benthic foraminiferal counts include both calcareous and agglutinated species. Where sufficient core material was available the sample depths correspond to the TOC and biomarker samples. The foraminiferal samples were weighed and wet sieved at

305 63 µm. The >63 µm fraction was counted wet, submerged in a 'storage' solution of 70 % distilled water and 30 % ethanol with baking soda to preserve fragile calcareous and agglutinated tests. A wet splitter was used when necessary to achieve a count of at least 200-300 benthic foraminifera. Planktonic foraminifera were counted in the benthic split. Equivalent dry weights of the foraminiferal samples were calculated using the wet weights of the samples and the wet and dry weights of other samples from the same depths. That way, the numbers of benthic and planktonic foraminifera per gram of dry sediment could be

310 calculated without drying the samples. Foraminiferal fluxes were calculated using the samples DBD and LSR and reported in

specimens cm^{-2} yr^{-1}, where the depth of the biomarker and foraminiferal samples were not identical, the DBD was linearly interpolated between neighbouring biomarker samples.

4. Results

The results of organic constituents and foraminiferal abundances in OD1507-03TC-41GC-03PC are presented on depth, to account for the bottom ca. 1.5 m of the core, where sediment ages are unconstrained (Reilly et al., 2019). This also allows to compare the data to the sedimentary facies in OD1507-03TC-41GC-03PC, characteristic of the glacial dynamics in the fjord.

4.1 HBI biomarker concentrations

IP$_{25}$ and HBI II were analysed in 100 samples with an average depth resolution of 5.5±1.8 cm and temporal resolution of 99±45 years. Both biomarkers were present in all samples, with an overall range of 0.3-30.0 ng g^{-1} sed for IP$_{25}$ and 0.6-83.0 ng g^{-1} sed for HBI II and fluxes of 0.2-3.0 ng cm^{-2} yr^{-1} and 0.3-8.0 ng cm^{-2} yr^{-1}, respectively (Fig. 3F, G). HBI concentrations normalized to the amount of sediment follow the biomarker concentrations normalized to the TOC content of the samples (Supplementary Fig. 3). A significant positive correlation was found for IP$_{25}$ and HBI II (R^2 = 0.95 [0.84; 0.97], n=100), in line with co-production of these two biomarkers (Brown et al., 2014). Sedimentary unit 3, is marked by very low IP$_{25}$ and HBI II concentrations (Fig. 3F, G). Both biomarker concentrations increase stepwise, with a first increase at 515 cm corresponding to the transition from sedimentary units 3 to 2 (Reilly et al., 2019). The second increase in biomarker concentrations at 405 cm precedes the sedimentary unit boundary (1C/2) by ~5 cm and is followed by an interval of highly variable IP$_{25}$ and HBI II concentrations and fluxes until 320 cm (Fig. 3F, G). From 260 cm, a steep increase in IP$_{25}$ and HBI II concentrations and fluxes culminates in peak concentrations at 199 cm followed by peak fluxes at 189 cm (Fig. 3F, G). Subsequently a two-step decrease in all HBI concentrations and fluxes is observed between 154 cm and 199 cm, spanning the transition of sedimentary units 1C and 1B at ~165 cm (Reilly et al., 2019) (Fig. 3F, G). At 154 cm, a sharp increase in IP$_{25}$ marks the onset of a second interval with sustained high concentrations between 154 cm and 70 cm. IP$_{25}$ fluxes increase simultaneously, but decrease prior to the concentrations at 89 cm in connection with a decrease in the LSR (Fig. 3A, G). HBI II concentrations remain relatively low throughout lower sedimentary unit 1B, while the fluxes follow the IP$_{25}$-flux trend (Fig. 3F, G). At 70 cm, however, IP$_{25}$ and HBI II concentrations and fluxes drop simultaneously, preceding the transition from sedimentary units 1B to 1A by ~7 cm (Fig. 3F, G). HBI biomarker concentrations and fluxes remain low throughout unit 1A, with a minor increase around 25 cm (Fig. 3F, G).
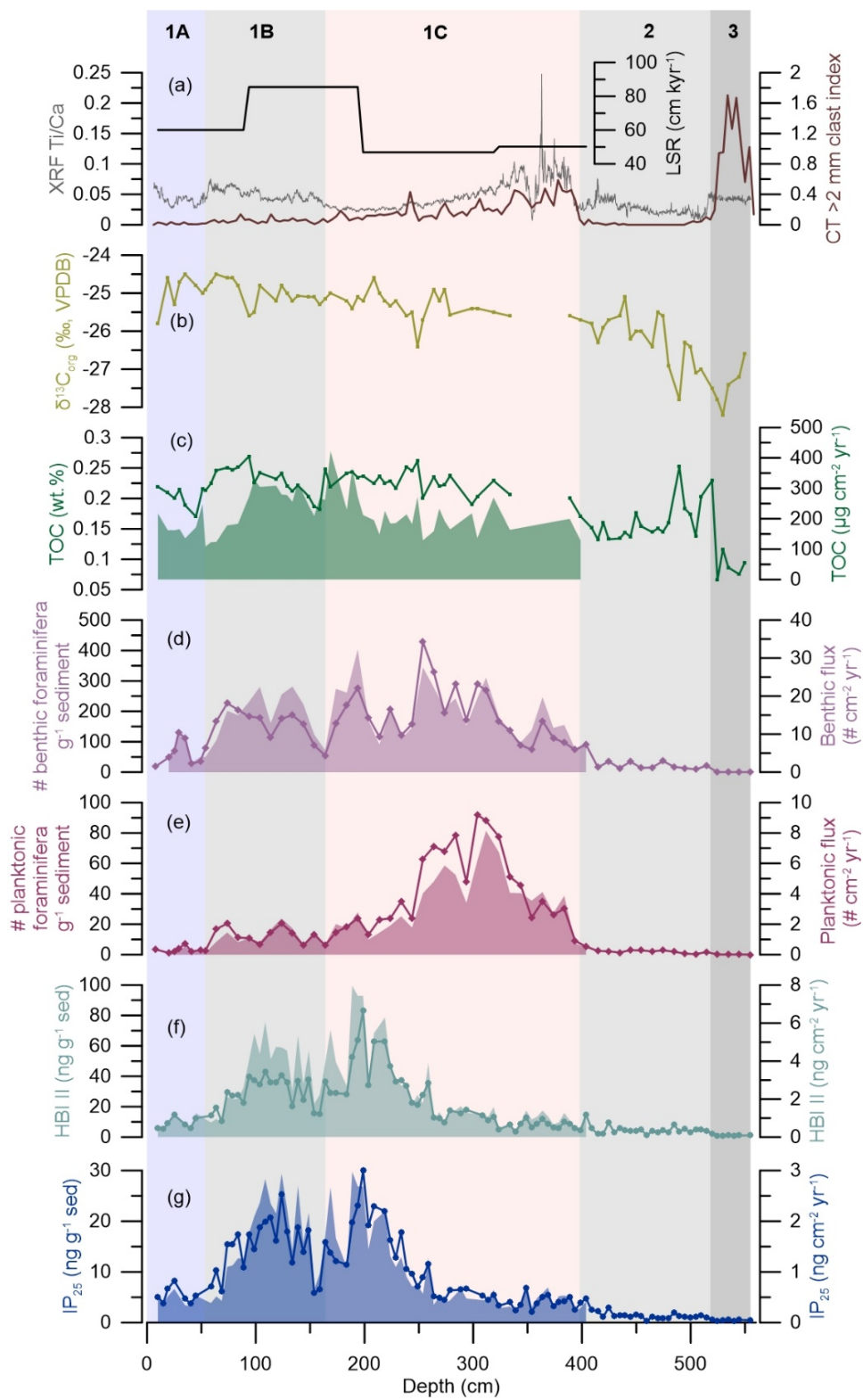
Figure 3. HBI biomarker, TOC, and foraminiferal results from OD1507-03TC-41GC-03PC. From the top to the bottom: (a) Linear sedimentation rates (LSR; black), the XRF Ti/Ca ratio (grey), and the CT >2 mm clast index (brown) (Reilly et al., 2019). (b) TOC carbon isotopic values ($\delta^{13}C_{org}$ ‰, VPDB; light green). (c) TOC fluxes (green, filled in area) and TOC concentrations (green line). (d) Benthic foraminiferal fluxes (purple, filled in area) and benthic foraminiferal abundance in individuals per g sediment (purple line with diamonds). (e) Planktonic foraminiferal fluxes (crimson, filled in area) and planktonic foraminiferal abundance in individuals per g sediment (crimson line with diamonds). (f) HBI II fluxes (turquoise, filled in area) and absolute concentration (turquoise line with dots) normalised to the amount of extracted sediment (ng g^{-1} sed.). (g) IP$_{25}$ fluxes (blue, filled in area) and absolute concentration (blue line with dots) normalised to the amount of extracted sediment (ng g^{-1} sed.). Fluxes do not extend beyond ~400 cm, as this depth corresponds to the lowermost available radiocarbon date (Reilly et al., 2019). The vertical background fill indicates the lithological units (1A-1C, 2, 3) at OD1507-03TC-41GC-03PC (Reilly et al., 2019).

The ratio of HBI II and IP$_{25}$ (DIP$_{25}$) has previously been used as an indicator for sea surface temperature (SST) and thus as a tracer of warmer water masses (Hörner et al., 2016; Xiao et al., 2013), in line with higher temperatures being more favourable for the synthesis of double bonds. Other studies, however, did not find a relationship between DIP$_{25}$ and SST and propose instead that a steady DIP$_{25}$ reflects stable sea-ice conditions, while a variable DIP$_{25}$ indicates more unstable sea-ice conditions (Belt and Müller, 2013; Cabedo-Sanz et al., 2013). In outer Petermann Fjord, the DIP$_{25}$ ratio is low throughout sedimentary unit 3 and rises before the unit3/unit 2 boundary (Supplementary Fig. 4). This is followed by the highest recorded DIP$_{25}$ values between 430 cm and 520 cm in unit 2. At 430 cm a sharp decline in DIP$_{25}$ values marks the onset of a 110 cm long section with relatively low but variable DIP$_{25}$ values ($\sigma^2 = 0.41$). At 320 cm, a small increase in DIP$_{25}$ is followed by a relatively steady decline throughout upper unit 1C, unit 1B, and unit 1A (Supplementary Fig. 4). This coincides with reduced variance in the data ($\sigma^2 = 0.26$).

4.2 Sterol biomarker concentrations

Sterol biomarkers were determined on 94 samples with a depth and temporal resolution of 5.7±2.3 cm and 102±51 years, respectively. We measured brassicasterol, dinosterol, and cholesterol (hereinafter grouped as marine sterols) and campesterol and β-sitosterol (hereinafter grouped as terrestrial sterols). All sterols were present consistently throughout the core (Table 3). There are minor differences in the temporal evolution of sterol concentrations normalized to the amount of sediment extracted and to the TOC content of the samples (Supplementary Fig. 3). These are especially apparent in the dinosterol, campesterol, and β-sitosterol concentrations. The differences are focused on the lower part of the record (400-500 cm), where Petermann Fjord is influenced by enhanced influx of terrestrial organic carbon (see section 5.1). Thus, we use sterol concentrations normalized to the extracted sediment mass and the resulting fluxes to make inferences about past environmental changes. One sample at ~319 cm has β-sitosterol concentrations three times higher than the average, while all other sterol concentrations fall within the reported range (Supplementary Fig. 5). It is not clear why the β-sitosterol concentrations are so high in this specific sample. Thus, we have excluded this sample from all further analyses and interpretations. Cholesterol is significantly correlated with dinosterol ($R^2 = 0.90$ [0.64; 0.98], n = 93) and brassicasterol ($R^2 = 0.93$ [0.75; 0.98], n = 93), in line with a predominantly marine source of cholesterol in Petermann Fjord. Further, the marine sterols show a good correlation with the IP$_{25}$ concentrations (IP$_{25}$-brassicasterol: $R^2 = 0.82$ [0.62; 0.92], n = 93, IP$_{25}$-cholesterol: $R^2 = 0.89$ [0.69; 0.96], n = 93, IP$_{25}$-dinosterol:

$R^2 = 0.82$ [0.56; 0.93], n = 93), suggesting an important role of sea ice for the regional marine primary productivity throughout the record.
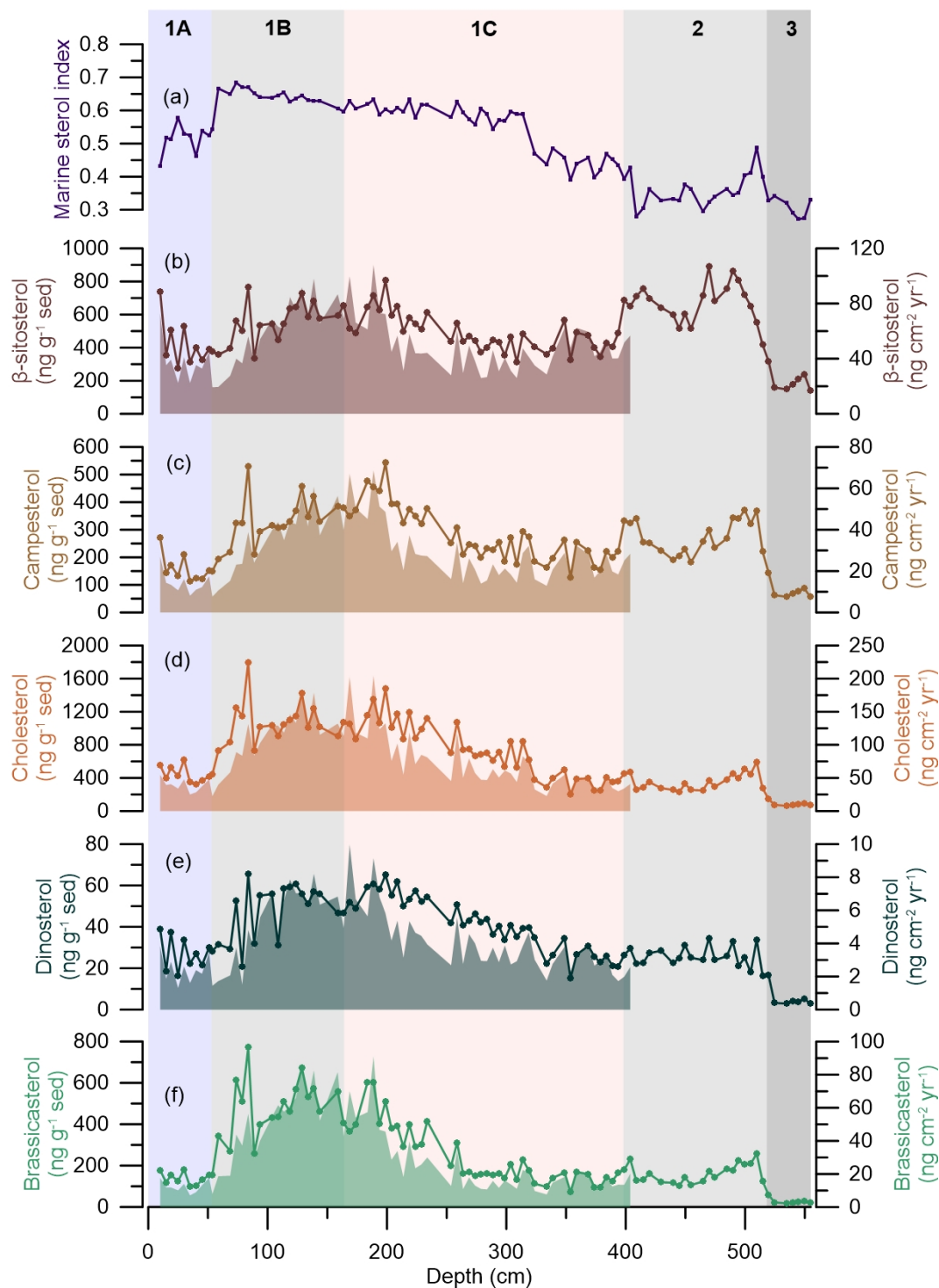
Figure 4. Sterol biomarker results at OD1507-03TC-41GC-03PC. From the top to the bottom: (a) Marine sterol index (sum of marine sterols/sum of all sterols) (purple line). (b) β-sitosterol fluxes (brown, filled in area) and absolute concentration (brown line with dots) normalised to the amount of extracted sediment (ng g^{-1} sed.). (c) Campesterol fluxes (light brown, filled in area) and absolute concentration (light brown line with dots) normalised to the amount of extracted sediment (ng g^{-1} sed.). (d) Cholesterol fluxes (orange-brown filled in area) and absolute concentration (orange-brown line with dots) normalised to the amount of extracted sediment (ng g^{-1} sed.). (e) Dinosterol fluxes (dark green, filled in area) and absolute concentration (dark green line with dots) normalised to the amount of extracted sediment (ng g^{-1} sed.). (f) Brassicasterol fluxes (light green, filled in area) and absolute concentration (light green line with dots) normalised to the amount of extracted sediment (ng g^{-1} sed.). Fluxes do not extend beyond ~400 cm, as this depth corresponds to the lowermost radiocarbon date (Reilly et al., 2019). The vertical background fill indicates the lithological units (1A-1C, 2, 3) at OD1507-03TC-41GC-03PC (Reilly et al., 2019).

Similar to the HBIs, the concentrations of all sterols increase at the transition from sedimentary units 3 to 2 with the most significant increase observed in β-sitosterol and campesterol (Fig. 4B, C). Both terrestrial sterols are characterized by a double peak throughout sedimentary unit 2, followed by a decline at the 1C/2 boundary, while the concentrations of marine sterols remain relatively stable throughout this interval (Fig. 4). Throughout unit 1C an increase in the cholesterol and dinosterol concentrations is observed from 350 cm, while their fluxes, alongside all other sterol concentrations remain low until 260 cm (Fig. 4D, E). Peak concentrations are reached between 199 cm and 189 cm, followed by a slight decrease in all sterol concentrations and a recovery during lower sedimentary unit 1B (Fig. 4). Simultaneously, sterol fluxes are at their highest between 94 cm and 194 cm, corresponding to the interval of maximum LSR (Fig. 4). While the sterol fluxes decrease from 94 cm, concentrations peak from 74-84 cm, followed by a sharp decrease prior to the transition from sedimentary units 1B to 1C. Unit 1C is characterized by overall low sterol concentrations and fluxes (Fig. 4).

For further insight into the environmental factors driving sterol variability, the marine sterol index (sum of marine sterols/sum of all sterols) was determined (Stein et al., 2017). This indicates that sedimentary units 3, 2, and the lowermost unit 1C have a higher relative concentration of terrestrial sterols, with a slight increase in the relative concentration of marine sterols just prior to the 2/1C boundary (Fig. 4A). The relative concentration of marine sterols increases between 314 cm and 59 cm, followed by a decrease at the boundary of sedimentary units 1A/1B (Fig. 4A).

Table 3. Ranges of sterol biomarker concentrations and fluxes in OD1507-03TC-41GC-03PC

Biomarker	Min. concentration (ng g^{-1} sed)	Max. concentration (ng g^{-1} sed)	Min. flux (ng cm^{-2} yr^{-1})	Max. flux (ng cm^{-2} yr^{-1})
Brassicasterol	17.6	771.1	7.1	91.0
Dinosterol	2.8	65.7	1.3	10.0
Cholesterol	62.4	1796.2	22.6	204.4
Campesterol	55.9	542.6	7.6	68.6
β-sitosterol	139.4	890.5	19.3	107.9

4.3 Total organic carbon (TOC) concentration and TOC carbon isotopes ($\delta^{13}C_{org}$)

The overall amount of TOC in OD1507-03TC-41GC-03PC is very low, varying between 0.1 wt.% and 0.3 wt.% (Fig. 3C). Between 289-394 cm and at 109 cm, samples recorded high TOC (0.3-1.8 wt.%) in combination with low $\delta^{13}C_{org}$ (-26.2-30.4 ‰), suggesting incomplete inorganic carbonate removal during sample processing. The interval between 289 cm and 394 cm is associated with high Ti/Ca ratios and IRD delivery to the core site, indicating increased glacial sedimentation in outer Petermann Fjord (Reilly et al., 2019) (Fig. 3A), which might have been associated with input of detrital carbonates. Thus, these samples have been removed from the TOC and $\delta^{13}C_{org}$ record (Fig. 3B and C).

The lowest TOC is encountered in sedimentary unit 3, followed by a sharp increase prior to the boundary of sedimentary units 3 and 2 at 520 cm depth. The lower unit 2 is characterized by large variability in the TOC content with two peaks at 520 cm and 490 cm, while the upper sediments of the same unit have a more stable TOC content around 0.15 wt.% (Fig. 3C). From 409 cm a steady increase of TOC into sedimentary unit 1C is observed. The TOC content in sedimentary units 1C, 1B, and 1A varies between 0.17 and 0.27 wt.% with local maxima around 250 cm and 94 cm and minima at 159 cm and 45 cm (Fig. 3C). TOC fluxes throughout these units vary between 109 and 422 µg cm^{-2} yr^{-1} with maximum fluxes from 94-194 cm, corresponding to the interval of maximum LSR. After 94 cm TOC fluxes decrease towards the boundary of sedimentary units 1B and 1A with minimum fluxes recorded at 54 cm and flux values similar to unit 1C throughout unit 1A (Fig. 3C).

The $\delta^{13}C_{org}$, measured on the same material as TOC, varies between -24.5 ‰ and -28.2 ‰. The lowest values are observed in sedimentary units 3 and 2 with minima at 490 cm and 530 cm and a relatively steady rise throughout the latter (Fig. 3B). Sedimentary units 1C, 1B, and 1A are marked by $\delta^{13}C_{org}$ values between -26.4 ‰ and -24.5 ‰ with local minima at 249 cm, 159 cm, and 10 cm (Fig. 3B).

4.4 Benthic and planktonic foraminiferal concentrations

The benthic and planktonic foraminiferal abundances vary between 0 and 429 specimens g^{-1} sediment and 0 and 92 specimens g^{-1} sediment, respectively (Fig. 3D, E). This corresponds to benthic and planktonic fluxes of 3-32 specimens cm^{-2} year^{-1} and 0-8 specimens cm^{-2} year^{-1} (Fig. 3D, E). In sedimentary units 2 and 3, benthic and planktonic foraminiferal abundances are low. Both benthic and planktonic abundances increase near the unit 2/unit 1C boundary, at 404 cm and 384 cm depth, respectively. Unit 1C is characterized by the highest overall foraminiferal abundances and fluxes with planktonic abundance and fluxes peaking between 304 cm and 312 cm prior to the benthic abundance, which peaks at 254 cm (Fig. D, E3). Planktonic foraminifera abundances and fluxes decline from 250 cm in unit 1C and continue at low values through unit 1B and are nearly absent in unit 1A (Fig. 3E). Benthic foraminiferal abundances and fluxes are more variable, but reach their lowest abundance in unit 1A (Fig. 3 D).

5. Discussion

5.1 Holocene variability in organic carbon sources and sea-ice dynamics in Petermann Fjord

Organic carbon (C_{org}) in Petermann Fjord is derived from a variety of sources, including in situ pelagic and sympagic production, advection of marine organic matter, and input of both modern and ancient C_{org} from the surrounding landmasses. While HBI concentrations are only marginally influenced by the addition of terrestrial C_{org}, sterols are important constituents in both marine and terrestrial primary producers (Belicka et al., 2004; Rontani et al., 2014; Volkman, 1986, 2003; Volkman et al., 1993, 2000; Yunker et al., 1995) (Table 2). Thus, in combination with $\delta^{13}C_{org}$, they can provide information on the dominant C_{org} source.

Sedimentary unit 3 represents grounding zone proximal sedimentation, associated with the deglacial retreat of PG into the fjord (Jakobsson et al., 2018; Reilly et al., 2019). This is in line with very low biomarker and TOC concentrations, and near absence of benthic and planktonic foraminifera (Fig. 5A-D), suggesting reduced primary productivity under an ice shelf/thick sea-ice cover and/or high sedimentation rates close to the grounding zone diluting the concentrations of organic constituents and marine microfossils close to the margin of a retreating glacier. Both sedimentary unit 3 and 2 are beyond the lowermost available radiocarbon age, which is why the influence of sedimentation rates on the biomarker and TOC concentrations cannot be assessed. The low marine sterol index throughout sedimentary unit 3 indicates that the C_{org} input was likely dominated by terrestrial sources, supported by low $\delta^{13}C_{org}$ values, characteristic of terrestrial vegetation in high latitudes (-26 ‰ to -28 ‰) (Ruttenberg and Goñi, 1997) (Fig. 3B). Where Washington and Hall Land border Petermann Fjord they are characterized by sedimentary rocks of lower Paleozoic age, primarily composed of shallow marine carbonates and evaporites (Dawes et al., 2000; Harrison et al., 2011). These contain ancient biomass that can be traced in marine sediments. The thermal maturity of these rocks, however, indicates that fossil sterols will have been, to a large part, degraded to steranes (Parnell et al., 2007), not measured as part of this study. Thus, the increased abundance of terrestrial sterols in sedimentary unit 3 is most likely related to input of fresh terrestrial organic material. Campesterol and β-sitosterol are dominant in vascular plants (such as herbs), but are also found in mosses and lichens (Matsuo and Sato, 1991; Safe et al., 1975), common to the high Arctic tundra. The deglacial retreat of PG occurs relatively late during the deglaciation of northern Greenland (<7,600 cal yrs BP) (Jakobsson et al., 2018), falling into the regional Holocene Thermal Maximum (HTM; ca. 11,000-5,500 cal yrs BP) (Kaufman et al., 2004) when adjacent Washington Land was already deglaciated (Ceperley et al., 2020) and pollen records from northern Greenland and Ellesmere Island suggest a more productive terrestrial Arctic ecosystem (Gajewski, 2015; Mode, 1996). This supports enhanced input of fresh terrestrial C_{org} to Petermann Fjord in response to glacial erosion and enhanced meltwater drainage of surrounding landmasses during the deglacial retreat of PG.
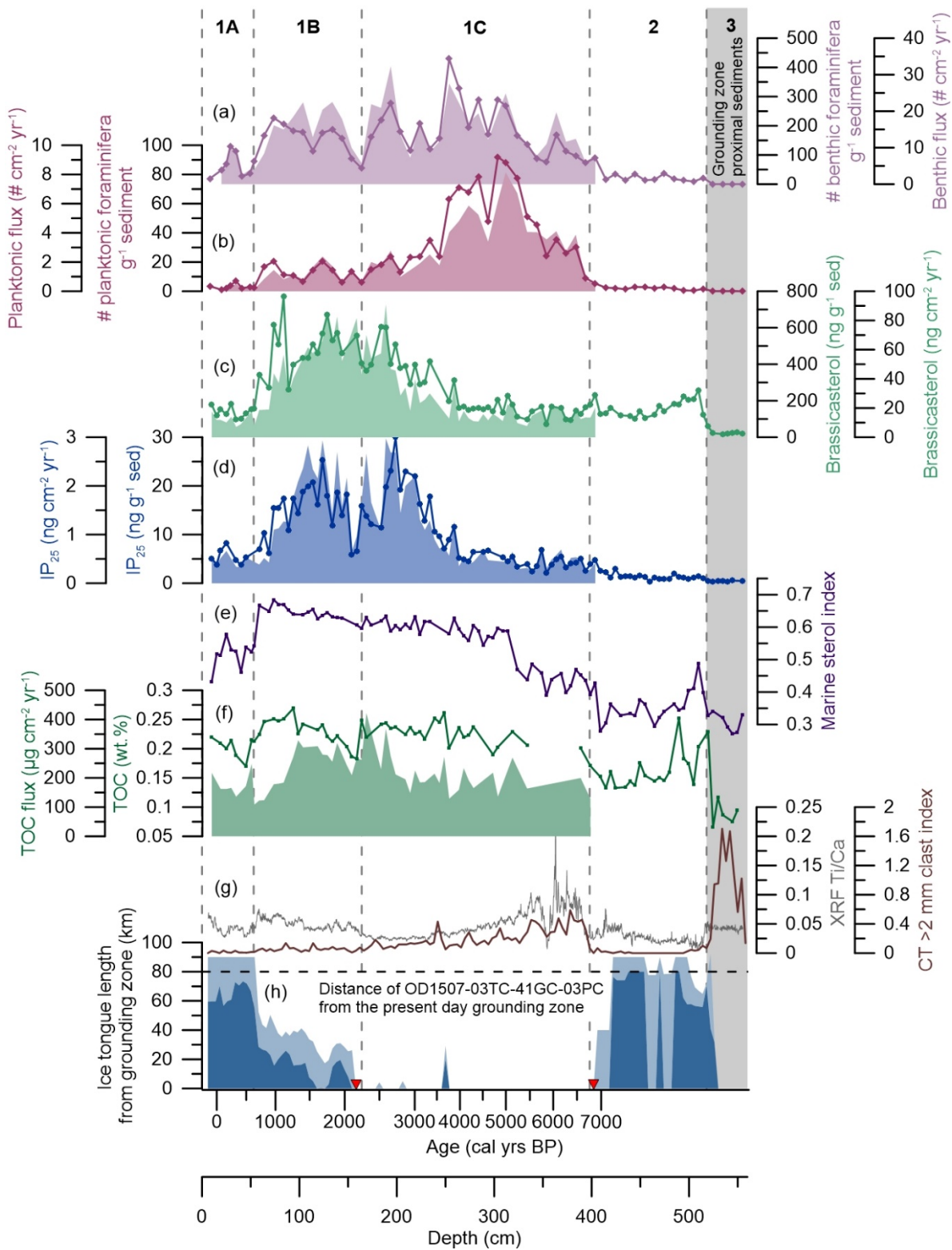
Figure 5. Temporal changes in the environmental conditions in Petermann Fjord. From the top to the bottom: (a) Benthic foraminiferal fluxes (purple, filled in area) and benthic foraminiferal abundance in individuals per g sediment (purple line with diamonds). (b) Planktonic foraminiferal fluxes (crimson, filled in area) and planktonic foraminiferal abundance in individuals per g sediment (crimson line with diamonds). (c) Brassicasterol fluxes (light green, filled in area) and absolute concentration (light green line with dots) normalised to the amount of extracted sediment (ng g^{-1} sed.). (d) IP$_{25}$ fluxes (blue, filled in area) and absolute concentration (blue line with dots) normalised to the amount of extracted sediment (ng g^{-1} sed.). (e) Marine sterol index (sum of marine sterols/ sum of all sterols) (purple line). (f) TOC fluxes (green, filled in area) and TOC concentrations (wt. %, green line). (g) XRF Ti/Ca ratios (grey) and the CT >2 mm clast index (brown) (Reilly et al., 2019). (h) Reconstruction of the Holocene ice tongue extent (minimum extent in dark blue, maximum extent in light blue) in Petermann Fjord in km from the grounding zone (Reilly et al., 2019). OD1507-03TC-41GC-03PC is located 80 km from the present day grounding zone (black dashed line). Lithogenic units (1A-1C, 2, 3) in sediment core OD1507-03TC-41GC-03PC are indicated with dashed vertical lines; grounding zone proximal sedimentation (unit 3) is indicated with a grey vertical bar. The red triangles on the x-axes indicate the timing of the ice tongue break-up (~6,900 cal yrs BP) and the late Holocene inception of a small ice tongue (~2,200 cal yrs BP) (Reilly et al., 2019).

Mapped submarine landforms suggest that the retreat of PG into the fjord was rapid, driven by ice cliff instability and promoted by the retrograde slope of the outer fjord sill (Jakobsson et al., 2018). An inner sill (Tinto et al., 2015) ~30 km seaward of the present day grounding zone (Reilly et al., 2019) likely halted the retreat, allowing for the formation of an extensive ice tongue associated with the laminated, IRD-poor lithofacies of unit 2 (Reilly et al., 2019). The transition from units 3 to 2 is marked by an increase in all biomarkers, TOC, and benthic and planktonic foraminiferal abundances (Fig. 5), suggesting an overall increase in C$_{org}$ input to outer Petermann Fjord and/or lower sedimentation rates in response to the larger distance of the core site from the grounding zone. The marine sterol index remains low, suggesting continued dominance of terrestrial versus marine sterols, while increasing δ^{13}C$_{org}$ values indicate enhanced importance of marine C$_{org}$ sources to Petermann Fjord. Thus, compared to sedimentary unit 3, the organic matter in sedimentary unit 2 was likely derived from more varied sources, including in situ/advected marine C$_{org}$ and terrestrial C$_{org}$. This supports a marginal/sub-ice tongue regime in outer Petermann Fjord with no or only intermittent sympagic and pelagic primary productivity in the fjord and low food supply to sustain benthic productivity (Jennings et al., 2020).

The early Holocene ice tongue of PG collapsed around 6,900 cal yrs BP (unit 2/unit 1C boundary), marked by the abrupt appearance of IRD clasts in sediments across Petermann Fjord (Reilly et al., 2019) (Fig. 5G). This is associated with an increase in the marine sterol index and TOC (Fig. 5), suggesting an increase in the C$_{org}$ delivery to outer Petermann Fjord and relatively more input of marine versus terrestrial sterols compared to previous sedimentary units. A second, larger, increase in the marine sterol index is evident at 5,100 cal yrs BP (Fig. 5E), contemporaneously with decreasing XRF Ti/Ca ratios and IRD flux (Reilly et al., 2019). This indicates reduced glacial erosion and calving activity or a decrease in the delivery of erosional products to outer Petermann Fjord from 5,100 cal yrs BP and dominant input of marine over terrestrial C$_{org}$, supported by δ^{13}C$_{org}$ (Fig. 5, Fig. 3). The marine sterol index remains high until ~600 cal yrs BP, while δ^{13}C$_{org}$ is high throughout the rest of the core, suggesting primarily delivery of marine-derived organic matter to outer Petermann Fjord during the mid-to-late Holocene.

The break-up of the early Holocene ice tongue is also associated with a small increase in the sedimentary IP$_{25}$ and HBI II concentrations, as well as an increase in the benthic and planktonic foraminiferal abundances. Between 6,900 cal yrs BP and 5,500 cal yrs BP, IP$_{25}$ fluxes are low but variable, indicating an unstable/variable sea-ice regime with predominantly reduced seasonal sea-ice concentration during spring and low rates of sympagic productivity. An unstable sea-ice regime is further

supported by variable DIP_{25} values (Supplementary Fig. 4). Alternatively, increased meltwater runoff related to the collapse of the ice tongue and associated retreat of PG, might have caused low/variable IP_{25} fluxes by creating environmental conditions unfavourable for IP_{25}-producing diatom species during times of increased freshwater discharge (Ribeiro et al., 2017). The simultaneous increase in TOC, benthic, and especially planktonic foraminiferal fluxes, however, supports a reduced seasonal sea-ice cover and a shift from a regime marginal to or below an ice tongue towards ameliorated conditions with a prolonged open water season and enhanced pelagic primary productivity in the fjord, allowing planktonic foraminifera to thrive (Fig. 5B). A reduced seasonal sea-ice cover is further supported by evidence of low sea-ice concentrations in Hall Basin until at least 6,000 cal yrs BP (Jennings et al., 2011b). Regional records from northern Greenland and the western Canadian Arctic Archipelago (CAA) demonstrate a HTM between 11,000 cal yrs BP and 5,500 cal yrs BP (Belt et al., 2010; Briner et al., 2016; England et al., 2008; Funder et al., 2011; Jennings et al., 2011b; Kaufman et al., 2004; Knudsen et al., 2008; Lecavalier et al., 2017; Ledu et al., 2010; Vare et al., 2009), associated with regional mean annual surface air temperatures 3±1°C higher than pre-industrial (1750 CE) (Lecavalier et al., 2017). Thus, reduced seasonal sea-ice concentrations in Petermann Fjord between 6,900 cal yrs BP and 5,500 cal yrs BP likely represent the late stages of the HTM in the northern Nares Strait region.

From ca. 5,800 cal yrs BP the increase in planktonic and benthic foraminiferal fluxes steepens, associated with less variable but still low IP_{25} fluxes from 5,500 cal yrs BP (Fig. 5A, B, and D). While benthic foraminifera respond to sea-ice changes via its influence on marine productivity and the resulting changes in food supply to the seafloor (Seidenkrantz, 2013), planktonic foraminiferal abundances have been shown to be highest in the open water region and along the ice margin, with only few individuals occurring under persistent sea ice (Carstens et al., 1997; Mayot et al., 2020; Pados and Spielhagen, 2014). In the modern environment of the northern Nares Strait and Petermann Fjord, planktonic foraminiferal abundances are very low in the fjord and much higher in the mobile sea ice regime of Nares Strait (Jennings et al., 2020), characterized by a shorter seasonal sea-ice season than outer Petermann Fjord (Fig. 2). Thus, high planktonic foraminiferal fluxes between 5,800 cal yrs BP and 3,600 cal yrs BP suggest sustained periods of seasonally open waters during summer, while the continuously low IP_{25} fluxes are consistent with reduced seasonal sea-ice concentrations and the absence of a sympagic spring bloom in outer Petermann Fjord (Fig. 5 D). Alternatively, IP_{25} production might have been suppressed due to lasting meltwater discharge into the fjord, resulting from the influence of the retreating PG on the outer fjord environment. However, both the >2 mm clast index and the XRF Ti/Ca ratios decrease throughout this interval (Reilly et al., 2019), suggesting a gradual reduction of the influence of glacial activity on the outer fjord (Fig. 5G).

From 3,900 cal yrs BP, IP_{25} fluxes increase steeply accompanied by an increase in all sterol fluxes (Fig. 4, Fig. 5D). This suggests a shift in the ecosystem in outer Petermann Fjord, associated with a transition from a regime dominated by pelagic primary productivity towards a regime characterized by enhanced sympagic productivity. Especially after 3,600 cal yrs BP, rapidly decreasing planktonic foraminiferal fluxes and steadily increasing IP_{25} fluxes indicate a progressively longer sea-ice season and enhanced sympagic productivity in outer Petermann Fjord (Fig. 5B, D). This falls into a period of long-term declining regional atmospheric temperatures recorded at Agassiz ice cap (Lecavalier et al., 2017) and in lake records in NW Greenland (Axford et al., 2019; Lasher et al., 2017). Neoglacial cooling has been observed in numerous marine and terrestrial

archives around Greenland and the wider North Atlantic region (e.g. England et al., 2008; Hansen et al., 2020; Jennings et al.,
2011a; Limoges et al., 2020; Vare et al., 2009), as a response to decreasing northern hemisphere summer insolation (Marcott
et al., 2013). Thus, enhanced seasonal sea-ice conditions in Petermann Fjord from 3,900 cal yrs BP (Fig. 5D), likely record the
onset of Neoglacial cooling in the northern Nares Strait region.

Peak IP_{25} fluxes around 2,500 cal yrs BP are associated with high fluxes of marine and terrestrial sterols as well as benthic
foraminifera, while planktonic foraminiferal fluxes are low (Fig. 4, Fig. 5A, B, D), indicating a prolonged seasonal sea-ice
cover with only short periods of open water during summer. From 2,500-2,100 cal yrs BP a two-stepped decrease in IP_{25} fluxes
is observed, of which the second decline is accompanied by a decrease in the TOC, benthic foraminiferal flux, and a small
decrease in the (already low) planktonic foraminiferal flux (Fig. 5A, B, F). A contemporaneous decline in all productivity
indicators and sea-ice biomarkers, suggests a restriction in the pelagic and sympagic primary productivity alike, most likely as
a response to further lengthening of the sea-ice season to near-perennial sea-ice cover. This interval precedes the late Holocene
inception of a small ice tongue in Petermann Fjord at 2,200-2,100 cal yrs BP, inferred from Ti/Ca ratios and the stacked >2
mm clast index from four cores in Petermann Fjord (Reilly et al., 2019). After 2,100 cal yrs BP, sea-ice biomarkers, TOC, and
benthic foraminiferal fluxes recover, while the planktonic foraminiferal abundance remains low (Fig. 5A, D, F), indicating an
ecosystem dominated by sympagic productivity and enhanced seasonal sea-ice cover, similar to the interval 3,600-2,500 cal
yrs BP. Compared to the deglacial PG ice tongue, the late Holocene ice tongue (<2,100 cal yrs BP) (Reilly et al., 2019) does
not seem to be associated with increased input of terrestrial organic matter to outer Petermann Fjord (Fig. 5). A possible
explanation could be lower atmospheric temperatures compared to the early Holocene (Lecavalier et al., 2017), associated
with a less diverse and more sparse terrestrial flora in the high Arctic (Gajewski, 2015) and decreased meltwater input. Another
reason could be increased distance of OD1507-03TC-41GC-03PC from the PG grounding zone during the late Holocene
(Reilly et al., 2019), resulting in reduced delivery of meltwater-derived C_{org}.

Around 1,300 cal yrs BP a sharp decline in IP_{25}, sterol, and TOC fluxes is observed, while the concentration of IP_{25} decreases
more gradually and the concentrations of sterols and TOC increase (Fig. 5). The sharp decrease in fluxes at this time coincides
with a large drop in the LSR (Fig. 3A), which might be biasing the flux data. Instead, the decline in biomarker fluxes at 950
cal yrs BP, accompanied by a decrease in the biomarker concentrations, seems to be a more reliable feature (Fig. 5). This is
associated with declining benthic foraminiferal fluxes, and followed by decreases in the planktonic foraminiferal and TOC
fluxes at 700 cal yrs BP (Fig. 5A, B, F), suggesting a return to near-perennial sea-ice conditions with reduced pelagic and
sympagic primary productivity, similar to the interval from 2,500-2,100 cal yrs BP. At ca. 600 cal yrs BP a rapid extension of
the Petermann ice tongue to its modern limits (Reilly et al., 2019), resulted in (at least intermittent) cover of the core site, in
line with low biomarker and foraminiferal fluxes between 600 cal yrs BP and the top of the core (Fig. 5). The latter indicates
low rates of primary productivity in a fjord, which is nearly completely covered by an ice tongue. This is further supported by
a decrease in the marine sterol index between 600 cal yrs BP and the top of the core, suggesting a relative decrease in the input
of marine organic matter (Fig. 5E). However, while there is a small decrease in the TOC at this time, there is no corresponding
decrease in the $\delta^{13}C_{org}$ (Fig. 3B), suggesting that marine C_{org} was still the main source of TOC in outer Petermann Fjord.
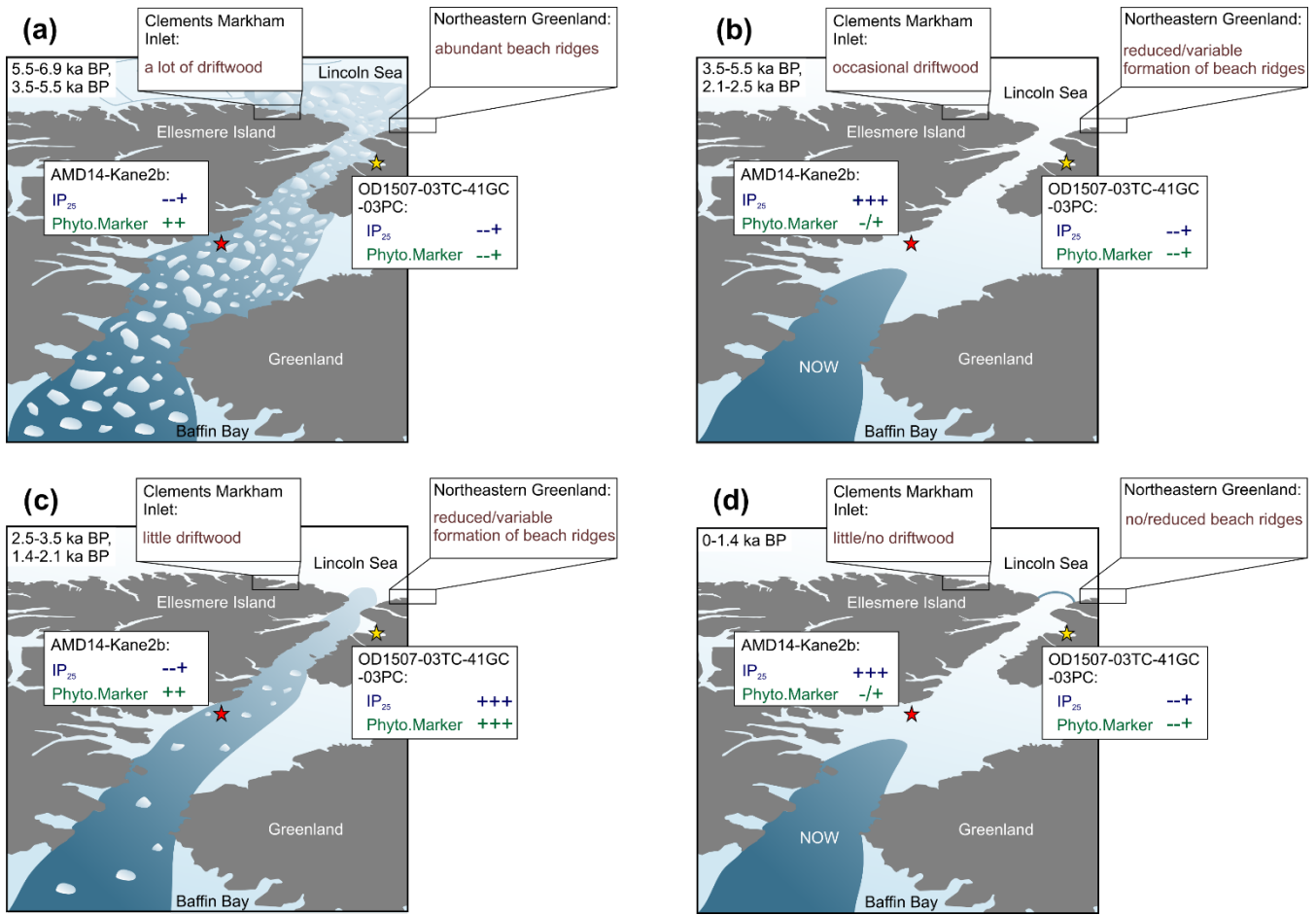
Figure 6. Schematic of spring sea-ice conditions and the respective sea-ice biomarker and primary productivity (HBI III at Kane2b, sterols at OD1507-03TC-41GC-03PC) indicator concentration patterns at OD1507-03TC-41GC-03PC (yellow star) and AMD14-Kane2b (red star), as well as driftwood delivery to CMI and beach ridge formation along the coast of north-eastern Greenland, based on different sea-ice and ice-arch scenarios in Nares Strait. In addition to the access to the coast, driftwood delivery also depends on the multiyear ice conditions in the Arctic Ocean, this is not considered in this simplified schematic. (a) No ice arch formation in Nares Strait resulting in year-round mobile sea ice, (b) Recurrent southern ice arch with landfast sea ice in Nares Strait and an open NOW, (c) Recurrent northern ice arch with locally formed sea ice remaining mobile in Nares Strait year-round, (d) Recurrent northern and southern ice arch with landfast sea ice in Nares Strait and a stable NOW. The time periods in the top left corner of each panel correspond to the proposed Holocene interval that experienced the respective conditions.

5.2 Nares Strait sea-ice dynamics over the last 7,000 cal yrs BP

Thus far, only one other biomarker-based sea-ice reconstruction, from station Kane2b in north-western Kane Basin, exists in Nares Strait for comparison with our records (Fig. 1) (Georgiadis et al., 2020). We propose that depending on the ice arch configuration in Nares Strait, Kane Basin and outer Petermann Fjord likely experience opposing conditions related to the proximity of the ice edge during spring/early summer (Supplementary Fig. 1), which is the dominant productivity season of sea-ice biomarkers. Kane2b is located near/under the southern ice arch in Nares Strait. Thus high sympagic productivity and IP$_{25}$ fluxes occur during times of a stable ice arch in Smith Sound and sea-ice edge conditions exist during spring/summer

585   (Georgiadis et al., 2020) (Fig. 6B, D). Georgiadis et al. (2020) interpret HBI III as generally indicating ice-laden/fresh surface waters, which can occur following the break-up of the southern ice arch and during times of mobile sea ice in Nares Strait. Thus, the southern ice arch scenario is likely associated with variable HBI III fluxes, depending on the seasonal timing of ice arch break-up. During the southern ice arch scenario, sea ice in Petermann Fjord does not break up until late summer/early autumn (Fig. 2), likely hindering a pronounced in-ice bloom related to MIZ conditions during spring/summer, resulting in

590   relatively low sea-ice and phytoplankton biomarker concentrations (Fig. 6B, D). In years when only the northern ice arch forms, sea ice formed locally in Nares Strait either remains mobile throughout the winter or breaks up during early spring. Under these conditions HBI III fluxes at Kane2b can be relatively high depending on the sea ice flux through Nares Strait during spring/summer, but no pronounced sympagic spring bloom occurs in Kane Basin (Fig. 6C). Instead, outer Petermann Fjord experiences spring MIZ conditions, as the formation of landfast ice in Petermann Fjord is independent of the formation

595   of landfast ice in Nares Strait (Fig. 2, Supplementary Fig. 1). This is likely associated with a significant spring sympagic bloom in outer Petermann Fjord and enhanced primary productivity related to the vicinity of the ice edge, resulting in increased concentrations of sea-ice and primary productivity biomarkers in outer Petermann Fjord (Fig. 6C). Periods with contemporaneously low concentrations of sea-ice and primary productivity biomarkers in Kane Basin and Petermann Fjord, point towards low spring sea-ice concentration in the entire Nares Strait, likely associated with a failure of both ice arches

600   (Fig. 6A).

In addition to the Kane Basin record, sea-ice dynamics around Ellesmere Island and NE Greenland have been inferred from records of driftwood delivery and beach ridge formation (England et al., 2008; Funder et al., 2011), providing context with respect to Holocene sea-ice conditions in the Arctic Ocean and Lincoln Sea. Driftwood is transported with Arctic multiyear ice and is deposited along the coastlines of northern Greenland and Ellesmere Island when landfast ice breaks up during

605   summer (Funder et al., 2011). The formation of beach ridges also depends on sufficient wave action and open water along the coast. Thus, abundant driftwood delivery to Ellesmere Island/north-eastern Greenland together with abundant formation of beach ridges is indicative of seasonally open waters along the coast (Fig. 6A). Sea-ice conditions with year-round landfast ice along the coast, on the other hand, will result in little or no driftwood landings and reduced formation of beach ridges (Fig. 6D). Lastly, variable ice conditions in Lincoln Sea result in occasional/little driftwood landings and reduced/variable formation

610   of beach ridges (Fig. 6B, C).

While the sediment core from station Kane2b covers the last 9,000 cal yrs BP (Georgiadis et al., 2020) (Fig. 1), Petermann Fjord did not deglaciate until ~7,600 cal yrs BP (Jakobsson et al., 2018) and the age model for OD1507-03TC-41GC-03PC is only constrained for the last 7,000 cal yrs BP. Thus, we focus on the interval from 6,900 cal yrs BP to the present. Between 6,900 cal yrs BP and 5,500 cal yrs BP, corresponding to the late stages of the regional HTM (Kaufman et al., 2004), sea-ice

615   biomarker and foraminiferal fluxes in Petermann Fjord and Kane Basin (Georgiadis et al., 2020), indicate reduced seasonal sea-ice occurrence (Fig. 7F, G). This corresponds to sparse driftwood delivery but abundant beach ridge formation around NE Greenland from 8,500-6,000 cal yrs BP, suggesting a minimum in Arctic multi-year ice and seasonally open water along the coast (Funder et al., 2011; Möller et al., 2010). Seasonally open water is further supported by maximum driftwood delivery to

Disraeli Fiord and Clements Markham Inlet (CMI) on Ellesmere Island (England et al., 2008) (Fig. 1, Fig. 7E). This is in line

620   with reduced seasonal sea-ice occurrence in Nares Strait, suggesting predominantly mobile sea ice with no or only occasional

ice arch formation and export of Arctic sea ice through Nares Strait (Fig. 6A) (Georgiadis et al., 2020).
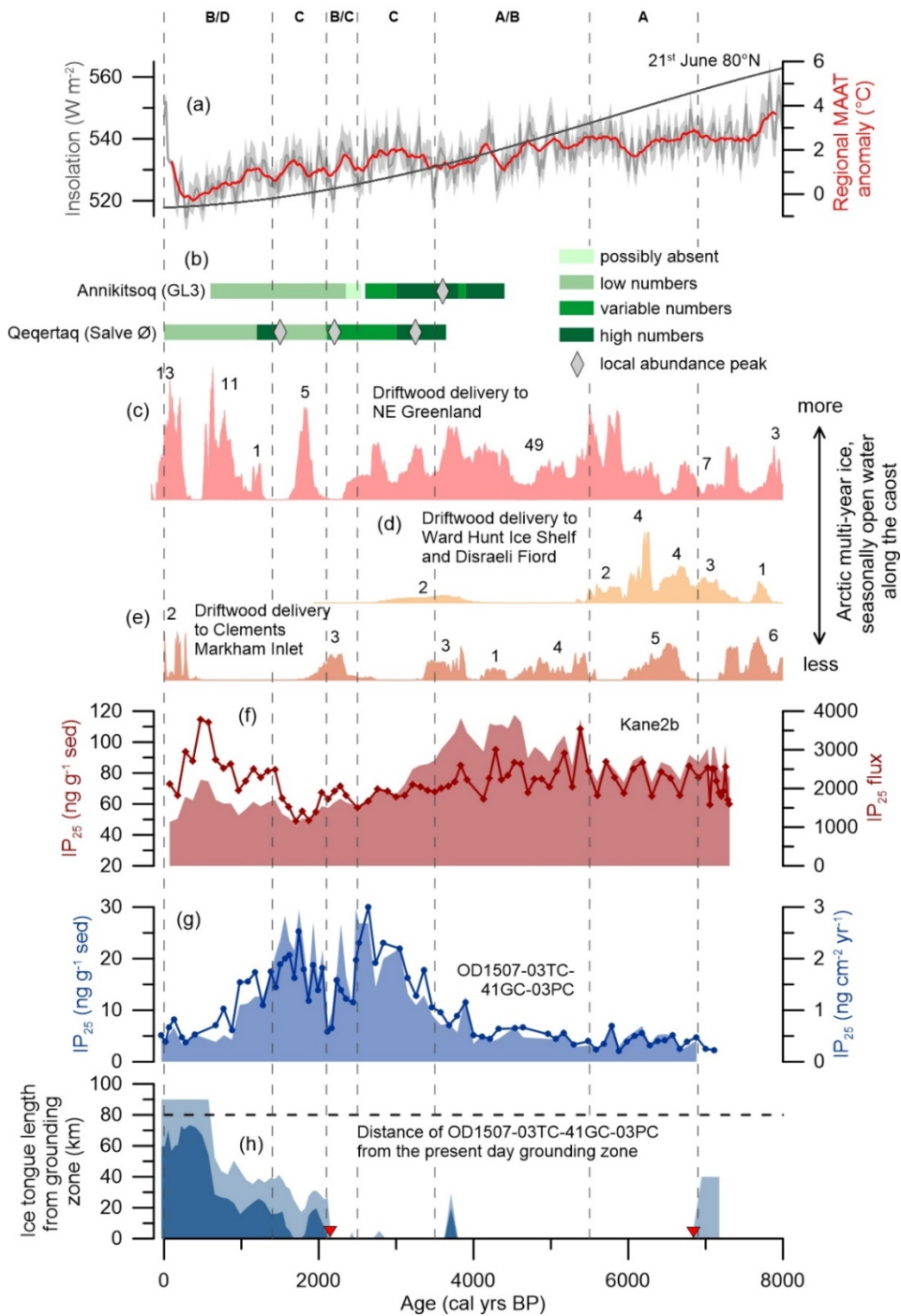
Figure 7. Holocene environmental changes in the wider Nares Strait region. From the top to the bottom: (a) Regional mean annual air temperature (MAAT) anomaly based on δ^{18}O at Agassiz ice cap at 25 yr resolution (Lecavalier et al., 2017) (grey line) including a 2σ uncertainty envelope (light grey filled in area) and a 5-pt running mean (red line), together with the 21st of June insolation at 80°N (dark grey). (b) Inferred variability in little auk numbers in seabird colonies at Annikitsoq and Qeqertaq (Davidson et al., 2018). (c) Cumulative probability distribution of calibrated ^{14}C ages of driftwood in NE Greenland north of 80°N (pink filled in area) (Funder et al., 2011). The numbers above the shaded area indicate the number of ages contributing to each block. (d) Cumulative probability distribution of calibrated ^{14}C ages of driftwood at Ward Hunt Ice Shelf and in Disraeli Fiord (yellow filled in area) (England et al., 2008). The numbers above the shaded area indicate the number of ages contributing to each block. (e) Cumulative probability distribution of calibrated 14C ages of driftwood in Clements Markham Inlet (yellow filled in area) (England et al., 2008). The numbers above the shaded area indicate the number of ages contributing to each block. (f) IP$_{25}$ fluxes (red, filled in area) and absolute concentrations (red line with diamonds) normalized to the amount of sediment extracted at AMD14-Kane2b (Georgiadis et al., 2020). (g) IP$_{25}$ fluxes (blue, filled in area) and absolute concentrations (blue line with dots) normalized to the amount of sediment extracted at OD1507-03TC-41GC-03PC. (h) Reconstruction of the Holocene ice tongue extent (minimum extent in dark blue, maximum extent in light blue) in Petermann Fjord in km from the grounding zone (Reilly et al., 2019). OD1507-03TC-41GC-03PC is located 80 km from the present day grounding zone (black dashed line). Corresponding to Fig. 6, interpretations of past ice arch dynamics in Nares Strait are marked with dashed vertical lines. The letters at the top correspond to the schematic scenarios in Fig. 6. The red triangles on the x-axes indicate the timing of the ice tongue break-up (~6,900 cal yrs BP) and the late Holocene inception of a small ice tongue (~2,200 cal yrs BP) (Reilly et al., 2019).

At 5,500 cal yrs BP increasing sea-ice biomarker fluxes in Kane Basin indicate a shift towards later sea-ice retreat and ice edge productivity, interpreted to reflect recurrent formation of the southern ice arch in Smith Sound/Kane Basin between 5,500 cal yrs BP and 3,000 cal yrs BP (Georgiadis et al., 2020) (Fig. 7F). A study of seabird colonies in the NOW region, suggests the arrival of little auk colonies in NW Greenland at 4,400 cal yrs BP, supporting the opening of the NOW lee of the Smith Sound ice arch during spring/summer (Davidson et al., 2018) (Fig. 7B). Little auk are zooplanktivore, feeding on the abundant copepod population of the NOW. Thus, large colonies of little auk in Greenland are only found in vicinity of productive polynyas, where open water is available for foraging upon their arrival in spring (Davidson et al., 2018). Productive and strong NOW conditions from 4,400 cal yrs BP are also inferred based on foraminiferal assemblages from the central polynya region (Jackson et al., 2021). Simultaneously, landfast sea ice started to form in Disraeli Fiord on northern Ellesmere Island from ~5,500 cal yrs BP, covering large parts of the coast by ~3,500 cal yrs BP (England et al., 2008), and shorter periods of open water and restricted beach ridge formation occur around NE Greenland (Funder et al., 2011). Even though this suggests an intensification of landfast sea-ice in the Lincoln Sea and the Arctic Ocean, open water along the NE Greenland coast was more abundant compared to today until at least 4,500 cal yrs BP (Funder et al., 2011). The period from 5,500-3,500 cal yrs BP, thus marks the transition from early Holocene warmth to Neoglacial cooling in the wider Nares Strait region. Compared to Kane2b, biomarker fluxes do not increase significantly at 5,500 cal yrs BP in outer Petermann Fjord (Fig. 7G). Instead, benthic and planktonic foraminiferal fluxes are at their highest between 5,500 cal yrs BP and 3,500 cal yrs BP (Fig. 6A, B), interpreted to reflect reduced seasonal sea-ice concentrations, the absence of a sympagic spring bloom, prolonged periods of seasonally open waters during summer, and increased pelagic primary productivity. Alternatively, the continuous influence of the retreating PG during this interval, potentially associated with increased meltwater discharge into the fjord, might have caused low concentrations of sea-ice biomarkers in outer Petermann Fjord (Ribeiro et al., 2017). Nonetheless, the high foraminiferal fluxes indicate conditions that differ from what would be expected in outer Petermann Fjord under a stable southern ice arch scenario (Fig. 6B). A possible reason for this could be enhanced seasonality, in particular enhanced winter cooling, due to the increasing

sea-ice extent in the Arctic Ocean (England et al., 2008; Funder et al., 2011), while summer insolation was still relatively high (though decreasing) compared to the late Holocene (Fig. 7). Modelling studies have shown that the loss of sea ice in the Arctic Ocean during the early Holocene counteracted the increased seasonality prescribed by insolation forcing, due to enhanced ocean-atmosphere heat flux during winter (Fischer and Jungclaus, 2011). The Arctic Ocean thus acted as a heat reservoir with increased latent and sensible heat flux during winter as a result of the reduced sea-ice cover (Fischer and Jungclaus, 2011). Conversely, decreasing summer insolation and the associated increase in Arctic Ocean sea-ice cover during the mid-Holocene (Fig. 7) strengthened the insulating effect of sea ice on the ocean and led to pronounced cooling during autumn/winter (Fischer and Jungclaus, 2011). Enhanced seasonality could explain the observed proxy patterns in Nares Strait between 5,500 cal yrs BP and 3,500 cal yrs BP, with an early seasonal break-up of the southern ice arch, leading to increased pelagic primary productivity in northern Nares Strait. This way, the spring ice edge bloom might still have occurred in the southern Nares Strait, followed by a rapid sea-ice retreat and open water conditions during summer/autumn, as recorded in outer Petermann Fjord. An early seasonal break-up of the southern ice arch is also supported by high HBI III fluxes, especially between 4,500 cal yrs BP and 3,500 cal yrs BP (Georgiadis et al., 2020). Thus, we suggest that this interval represents the transition from reduced sea-ice conditions and the lack of ice arches in Nares Strait during the late HTM towards more stable sea-ice conditions associated with the seasonal formation of a recurrent southern ice arch from at least ~4,400 cal yrs BP.

From 3,900 cal yrs BP, increasing IP_{25} fluxes in Petermann Fjord, attest to a shift in the primary productivity regime from predominantly pelagic to MIZ/sympagic primary productivity at 3,500 cal yrs BP. A similar increase in IP_{25} concentrations from ~4,000 cal yrs BP is also observed in the western CAA, in Barrow, Victoria, and Dease Strait (Belt et al., 2010; Vare et al., 2009), in line with enhanced seasonal sea-ice formation and the onset of regional Neoglacial cooling. Conversely, IP_{25} concentrations in Kane Basin decrease from ~4,000 cal yrs BP until 1,400 cal yrs BP (Fig. 7F), suggesting no stable southern ice arch in Smith Sound. Instead, the driftwood delivery to CMI ceases at 3,500 cal yrs BP (England et al., 2008). This likely indicates a regime shift in Nares Strait with the northern ice arch becoming more prominent between 3,500 cal yrs BP and 1,400 cal yrs BP (Fig. 6C). In years where only the northern ice arch forms, along strait winds in Nares Strait keep locally formed sea ice mobile year-round (Vincent, 2019), creating MIZ conditions in Petermann Fjord during spring/summer (Supplementary Fig. 1), in line with high IP_{25} concentrations. Between 2,500 cal yrs BP and 2,100 cal yrs BP biomarker fluxes in outer Petermann Fjord, suggest a shift towards near-perennial sea-ice conditions (Fig. 7G). This is associated with some driftwood landings in CMI (England et al., 2008) and a period of no driftwood or beach ridge occurrences in NE Greenland, suggesting perennial landfast ice (Funder et al., 2011). The numbers of little auks at Qeqertaq (Salve Ø) are variable during this time period, with a local peak in abundance at ~2,200 cal yrs BP (Davidson et al., 2018). In Kane Basin, IP_{25} fluxes are relatively low until ca. 1,400 cal yrs BP, however a minor peak (more pronounced in IP_{25} concentrations) can be observed between ca. 2,300 cal yrs BP and 2,000 cal yrs BP. This coincides with a period of low HBI III fluxes from ca. 2,700-2,100 cal yrs BP at Kane2b (Georgiadis et al., 2020). Georgiadis et al. (2020) interpret HBI III as indicating ice loaded fresh surface waters in relation to mobile sea ice/ice arch break-up in Nares Strait. A decrease in HBI III fluxes and concomitant small increase in IP_{25} could thus result from intermittent formation of the southern ice arch in Kane Basin and opening of the NOW,

consistent with the local abundance peak of little auks and sea-ice records from outer Petermann Fjord and north-eastern Greenland. Foraminiferal assemblages from the central NOW region (91-039-008P, Fig. 1) demonstrate a shift towards increased bottom water ventilation around 2,600 cal yrs BP (Knudsen et al., 2008), which could point towards strengthened polynya conditions and intensified brine formation in the NOW region. Unfortunately, however, no sediments were recovered at site 91-039-008P between 2,450 cal yrs BP and 1,100 cal yrs BP (Knudsen et al., 2008). Increased bottom water ventilation is also inferred from measurements of total sulphur at CASQ1 (Fig. 1) (Jackson et al., 2021). Simultaneously, calcareous foraminiferal abundances are low between 2,500-2,000 cal yrs BP at CASQ1 (Fig. 1) (Jackson et al., 2021). While this hinders unambiguous environmental interpretations, it could also be a sign of strong polynya conditions and formation of CO_2-rich brines, causing dissolution of the calcareous foraminiferal test and preservation of agglutinated species only (Jackson et al., 2021). Georgiadis et al. (2020) suggest that the period of mobile sea ice in Nares Strait between 3,500 cal yrs BP and 1,400 cal yrs BP was driven by a change in the dominant phase of the Arctic Oscillation (AO). The shift towards a positive AO between 3,000 cal yrs BP and 1,200 cal yrs BP (Darby et al., 2012) might have been associated with stronger along strait winds in Nares Strait. As ice arch formation in Nares Strait is a function of ice thickness, local wind stress, and atmospheric temperatures (Barber et al., 2001; Samelson et al., 2006), distinct atmospheric cooling spikes between ~2,500 cal yrs BP and ~1,900 cal yrs BP, recorded at Agassiz ice cap (Lecavalier et al., 2017), might have been responsible for the enhanced sea-ice concentration and the formation of an intermittent southern ice arch in Nares Strait between 2,500 cal yrs BP and 2,100 cal yrs BP (Fig. 7A).

After 2,100 cal yrs BP and until 1,400 cal yrs BP, the combined biomarker records in Nares Strait support a return to a more northern ice arch dominated sea-ice regime. This is supported by foraminiferal assemblages from the central NOW region, suggesting weaker polynya conditions from 1,800-1,400 cal yrs BP (Jackson et al., 2021). From 1,400 cal yrs BP onwards, IP_{25} fluxes in Kane Basin increase (Georgiadis et al., 2020), while they decline in Petermann Fjord (Fig. 7F, G) concomitant with high numbers of little auks at Qeqertaq (Salve Ø) (Davidson et al., 2018), suggesting a transition towards a more stable southern ice arch. These conditions are further consolidated from 950 cal yrs BP, where the sudden drop in sea-ice and primary productivity indicators in Petermann Fjord (Fig. 5, Fig. 7G) indicate near-perennial landfast sea ice in Nares Strait promoted by the recurrent formation of a southern ice arch. Driftwood is absent in CMI from 2,200-400 cal yrs BP (England et al., 2008), suggesting that the northern arch might have been a stable feature as well (Fig. 7E, Fig. 6D). Periods of double ice arching in Nares Strait are particularly stable (Ryan and Münchow, 2017), in line with the coldest Holocene temperatures recorded at Agassiz ice cap throughout this interval (Lecavalier et al., 2017). At ~600 cal yrs BP a large jump in the extent of the late Holocene ice tongue in Petermann Fjord to its modern (pre 2010) limits, suggests a regime marginal to or under an ice tongue in outer Petermann Fjord (Reilly et al., 2019) (Fig. 7H). Thus, further interpretations of the sea-ice environment in Nares Strait are hindered due to the influence of the ice tongue on primary productivity in Petermann Fjord.

5.3 Implications of sea ice for the formation and stability of the Petermann ice tongue

A recent study by Reilly et al. (2019) demonstrates that an extensive ice tongue in Petermann Fjord is a relatively recent feature compared to large parts of the Holocene. The final stage of the deglaciation in Petermann Fjord was characterized by the break-up of a deglacial ice tongue around 6,900 cal yrs BP, followed by a period of enhanced IRD and Ti/Ca ratios in the fjord sediments (6,900-3,500 cal yrs BP; Fig. 5G), indicating increased glacial sedimentation in outer Petermann Fjord. First at ~2,200 cal yrs BP a small ice tongue re-emerged, followed by gradual growth and a rapid expansion to its modern extent around 600 cal yrs BP (Reilly et al., 2019). Thus, the mid-to-late Holocene was marked by a ~4,700 year interval where no stable ice tongue existed in Petermann Fjord (Reilly et al., 2019). The presence of an ice tongue in Petermann Fjord is determined by the interplay of several factors, including the surface mass balance of PG, the loss of glacial ice by calving, and the basal melt rates. Local changes in sea-ice dynamics have the potential to influence both the basal melt rates and the stability of the calving front at PG. The latter depends on the formation and seasonal duration of landfast sea ice in Petermann Fjord, creating an ice mélange that stabilizes the calving front and reduces the length of the calving season (Amundson et al., 2010; Carr et al., 2015; Robel, 2017; Todd and Christoffersen, 2014). Along with the increase in IP$_{25}$ fluxes in outer Petermann Fjord, indicating a transition towards enhanced sea-ice conditions, from at least 3,500 cal yrs BP, a cessation of the IRD flux is observed in OD1507-03TC-41GC-03PC (Fig. 5D, G) (Reilly et al., 2019). This suggests a gradual decrease in the calving of icebergs from PG during the mid-Holocene. We propose that this was partly in response to the formation of seasonal landfast ice in the fjord, shortening the calving season (Fig. 6; Fig. 7). Sea ice also has the ability to influence the oceanic heat transport to Petermann Fjord, via modification to the circulation driven AAW inflow by regulating the wind stress at the atmosphere/ocean interface in Nares Strait (Shroyer et al., 2017). Under modern conditions, AAW inflow is enhanced at times of mobile sea ice in Nares Strait, while landfast sea ice results in decreased oceanic heat flux to Petermann Fjord (Shroyer et al., 2017). In addition to Nares Strait sea-ice conditions, subglacial runoff and glacial isostatic uplift of the outer fjord sill likely also influenced the inflow of AAW to Petermann Fjord across the Holocene (Bennike, 2002; Cai et al., 2017; Washam et al., 2019). Recurrent formation of a southern ice arch and seasonal formation of landfast sea ice, may have persisted in Nares Strait from 5,500-3,500 cal yrs BP, 2,500-2,100 cal yrs BP, and <1,400 cal yrs BP, based on the assessment of regional sea-ice records (England et al., 2008; Funder et al., 2011; Georgiadis et al., 2020, this study) (Fig. 6B, D). The interval from 5,500-3,500 cal yrs BP marks the transition from the HTM to Neoglacial cooling in the Nares Strait region. While records from southern Nares Strait suggest an opening of the NOW and spring ice edge conditions in Kane Basin from at least 4,400 cal yrs BP, records from outer Petermann Fjord indicate low sympagic but high pelagic productivity, suggesting prolonged periods of open water during summer (Fig. 5A, B, D). Increased seasonality, with early break-up of the southern ice arch and late seasonal sea-ice formation might be able to explain the observed patterns (section 5.3). Thus, unlike today, the formation of a southern ice arch between 5,500 cal yrs BP and 3,500 cal yrs BP did likely not lead to a prolonged landfast ice season in Nares Strait. Consequently, the longer mobile sea-ice season in Nares Strait might have contributed to AAW inflow to Petermann Fjord preventing the formation of an ice tongue throughout this interval.

Between 2,500 cal yrs BP and 2,100 cal yrs BP regional records of sea ice (England et al., 2008; Georgiadis et al., 2020, this study), seabird colonies (Davidson et al., 2018), and NOW dynamics (Jackson et al., 2021) suggest intermittent formation of a southern ice arch in Nares Strait, likely in response to regional atmospheric cooling spikes (Lecavalier et al., 2017). This interval spans the inception of a small late Holocene ice tongue in Petermann Fjord (Fig. 7H), suggesting that increased formation of landfast ice in Nares Strait may have reduced the oceanic heat flux to Petermann Fjord and stabilized the glacier front. Together with atmospheric cooling this likely aided the formation of a small ice tongue at ~2,200 cal yrs BP (Reilly et al., 2019). Similarly, the interval <1,400 cal yrs BP including the rapid growth of the Petermann ice tongue to its modern limits at ca. 600 cal yrs BP (Reilly et al., 2019). Regional sea-ice records indicate the onset of a more recurrent southern arch from ~1,400 cal yrs BP, with a further decrease in sea-ice and primary productivity markers in Petermann Fjord and a concurrent increase in IP_{25} in Kane Basin at 950 cal yrs BP implying the formation of more stable ice arch conditions and potentially even double ice-arching. Thus, both the inception of the ice tongue in Petermann Fjord at ~2,200 cal yrs BP and its rapid extension at 600 cal yrs BP are preceded by a transition towards stable southern ice arch conditions in the Nares Strait by 300-350 years (Fig. 7, Fig. 6B, D). More severe sea ice, with longer periods of landfast ice in Nares Strait, thus likely promoted ice tongue growth in Petermann Fjord, either directly via stabilizing the calving front or indirectly via changes to the inflow in modified AW. In light of the recent development, our data suggest that the emerging dominance of the northern ice arch associated with year-round mobile sea ice in Nares Strait and a shorter landfast sea-ice season in Petermann Fjord, will likely contribute to the destabilization of the ice tongue. Thus, a future reduction in landfast sea ice in Nares Strait and adjacent fjords would likely contribute to enhanced mass loss from the GrIS.

6. Conclusions

1. During the deglaciation (>6,900 cal yrs BP) outer Petermann Fjord experienced enhanced input of fresh terrestrial C_{org}, likely due to the late deglacial retreat of PG and increased glacial erosion during the early HTM, characterized by more productive Arctic tundra vegetation in northern Greenland and Ellesmere Island.

2. Following deglacial retreat of PG and break-up of the deglacial ice tongue in Petermann Fjord at 6,900 cal yrs BP, sea-ice biomarkers and productivity indicators in outer Petermann Fjord suggest reduced seasonal sea-ice occurrence and predominantly pelagic primary productivity until 5,500 cal yrs BP, corresponding to the late stages of the regional HTM. Together with other regional records, this suggests the lack of ice arches and export of sea ice from Lincoln Sea through Nares Strait.

3. The interval from 5,500-3,500 cal yrs BP marks the transition from the late stages of the HTM to the onset of Neoglacial cooling. This was likely associated with a formation of a southern ice arch and the opening of the NOW from at least ~4,400 cal yrs BP. However, an earlier seasonal break-up of the southern ice arch, compared to today, associated with a longer open water season, caused enhanced pelagic productivity in Nares Strait and seasonal coastal melt in CMI and around NE Greenland.

4. Between 3,500 cal yrs BP and 1,400 cal yrs BP (excluding 2,500-2,100 cal yrs BP) outer Petermann Fjord was marked by enhanced pelagic productivity suggesting a marginal ice zone location during early spring/summer in response to the northern Nares Strait ice arch becoming more prominent and locally formed sea ice remaining mobile in Nares Strait year-round. A stable northern ice arch throughout this interval is supported by the cessation of driftwood delivery to CMI.

5. From 2,500-2,100 cal yrs BP, declining sea-ice biomarker fluxes alongside declining productivity indicators in outer Petermann Fjord suggest a restriction of all primary productivity, likely as a result of near-perennial sea-ice cover. In combination with a small rise in the IP_{25} and a concomitant decrease in the HBI III fluxes in Kane Basin, strong NOW conditions, reappearance of driftwood at CMI, and a local abundance peak of little auk seabird colonies at Qeqertaq (Salve Ø), this suggest a transient return to a southern ice arch regime in Nares Strait. Georgiadis et al. (2020) suggest that a dominantly positive AO phase from 3,000-1,200 cal yrs BP, associated with stronger along strait winds in Nares Strait, might have physically prevented the formation of ice arches. Since ice-arch formation in Nares Strait also depends on atmospheric temperatures and sea-ice thickness, distinct atmospheric cooling spikes between 2,500 cal yrs BP and 1,900 cal yrs BP, might have exerted a positive feedback on sea-ice mechanics, counterbalancing the increased wind stress and enabling the formation of a southern ice arch.

6. The collective sea ice reconstructions in the Nares Strait and Lincoln Sea region indicate a return to a stable southern ice arch regime and potentially even double ice arching >1,400 cal yrs BP.

7. Our data demonstrates that the formation of landfast sea ice in Petermann Fjord and Nares Strait preceded major growth events of the Petermann ice tongue. This suggests that sea ice promotes an environment favourable for ice tongue growth, either directly or indirectly via stabilizing the glacier calving front and possibly decreasing the inflow of AAW to Petermann Fjord. Conversely, a reduction in the landfast sea-ice season in Nares Strait and adjacent fjords, as observed during the last decade, will likely contribute to destabilizing local ice tongues, which might result in enhanced mass loss from the GrIS in the future.

Data availability

The data presented as part of this manuscript is archived in the PANGAEA database and can be accessed via the following link https://doi.pangaea.de/10.1594/PANGAEA.929918.

Author contribution

The study was designed by HD and CP with help from BR and AJ. MJ led the Petermann Expedition and collected the core together with BR and AJ. HD carried out the sample processing and analyses for sea-ice biomarkers with help from MMJ. AJ carried out the processing and analyses for foraminiferal census counts. JO performed the TOC analyses. MJ, MG, and CP acquired funding for this study. HD prepared the manuscript with valuable contributions from all co-authors.

Competing interests

825   The authors declare that they have no conflict of interest.

Acknowledgements

We would like to thank the captain and crew, as well as the scientific party, on the Icebreaker *Oden* during *The Petermann 2015 Expedition*. Thank you to the Oregon State University Marine Geology Repository (OSU-MGR) for core archiving and sampling of the core. Further, we would like to thank Simon Belt and Lukas Smik for providing biomarker laboratory standards
830   and Trine Ravn-Jonsen and René Bjerregaard Madsen for laboratory support. This work was funded by the Aarhus University Research Foundation (AUFF-E-17-7-22 to Christof Pearce), the National Science Foundation Office of Polar Programs (Award 1417784 to Anne Jennings), the National Science Foundation Division of Ocean Sciences (1558679), and the Swedish Research Council (VR, 2016-04021 to Martin Jakobsson). We also thank the Swedish Polar Research Secretariat for supporting *The Petermann 2015 Expedition*. Lastly, we acknowledge the use of imagery from the NASA Worldview application
835   (https://worldview.earthdata.nasa.gov/), part of the NASA Earth Observing System Data and Information System (EOSDIS).

References

Amundson, J. M., Fahnestock, M., Truffer, M., Brown, J., Lüthi, M. P. and Motyka, R. J.: Ice mélange dynamics and implications for terminus stability, Jakobshavn Isbræ, Greenland, J. Geophys. Res., 115(F1), F01005, doi:10.1029/2009JF001405, 2010.

840   Ardyna, M. and Arrigo, K. R.: Phytoplankton dynamics in a changing Arctic Ocean, Nat. Clim. Chang., 10(10), 892–903, doi:10.1038/s41558-020-0905-y, 2020.

Axford, Y., Lasher, G. E., Kelly, M. A., Osterberg, E. C., Landis, J., Schellinger, G. C., Pfeiffer, A., Thompson, E. and Francis, D. R.: Holocene temperature history of northwest Greenland – With new ice cap constraints and chironomid assemblages from Deltasø, Quat. Sci. Rev., 215, 160–172, doi:10.1016/j.quascirev.2019.05.011, 2019.

845   Barber, D. G., Hanesiak, J. M., Chan, W. and Piwowar, J.: Sea-ice and meteorological conditions in Northern Baffin Bay and the North Water polynya between 1979 and 1996, Atmos. - Ocean, 39(3), 343–359, doi:10.1080/07055900.2001.9649685, 2001.

Belicka, L. L., Macdonald, R. W., Yunker, M. B. and Harvey, H. R.: The role of depositional regime on carbon transport and preservation in Arctic Ocean sediments, Mar. Chem., 86(1–2), 65–88, doi:10.1016/j.marchem.2003.12.006, 2004.

850   Belt, S. T.: Source-specific biomarkers as proxies for Arctic and Antarctic sea ice, Org. Geochem., 125, 277–298, doi:10.1016/J.ORGGEOCHEM.2018.10.002, 2018.

Belt, S. T. and Müller, J.: The Arctic sea ice biomarker IP_{25}: a review of current understanding, recommendations for future research and applications in palaeo sea ice reconstructions, Quat. Sci. Rev., 79, 9–25, doi:10.1016/j.quascirev.2012.12.001,

2013.

855   Belt, S. T., Massé, G., Rowland, S. J., Poulin, M., Michel, C. and LeBlanc, B.: A novel chemical fossil of palaeo sea ice: IP_{25}, Org. Geochem., 38(1), 16–27, doi:10.1016/J.ORGGEOCHEM.2006.09.013, 2007.

Belt, S. T., Vare, L. L., Massé, G., Manners, H. R., Price, J. C., MacLachlan, S. E., Andrews, J. T. and Schmidt, S.: Striking similarities in temporal changes to spring sea ice occurrence across the central Canadian Arctic Archipelago over the last 7000 years, Quat. Sci. Rev., 29(25–26), 3489–3504, doi:10.1016/j.quascirev.2010.06.041, 2010.

860   Belt, S. T., Brown, T. A., Rodriguez, A. N., Sanz, P. C., Tonkin, A. and Ingle, R.: A reproducible method for the extraction, identification and quantification of the Arctic sea ice proxy IP_{25} from marine sediments, Anal. Methods, 4(3), 705, doi:10.1039/c2ay05728j, 2012.

Belt, S. T., Cabedo-Sanz, P., Smik, L., Navarro-Rodriguez, A., Berben, S. M. P., Knies, J. and Husum, K.: Identification of paleo Arctic winter sea ice limits and the marginal ice zone: Optimised biomarker-based reconstructions of late Quaternary

865   Arctic sea ice, Earth Planet. Sci. Lett., 431, 127–139, doi:10.1016/J.EPSL.2015.09.020, 2015.

Belt, S. T., Brown, T. A., Smik, L., Tatarek, A., Wiktor, J., Stowasser, G., Assmy, P., Allen, C. S. and Husum, K.: Identification of C_{25} highly branched isoprenoid (HBI) alkenes in diatoms of the genus Rhizosolenia in polar and sub-polar marine phytoplankton, Org. Geochem., 110, 65–72, doi:10.1016/J.ORGGEOCHEM.2017.05.007, 2017.

Bennike, O.: Late Quaternary history of Washington Land, North Greenland, Boreas, 31(3), 260–272, doi:10.1111/j.1502-

870   3885.2002.tb01072.x, 2002.

Briner, J. P., McKay, N. P., Axford, Y., Bennike, O., Bradley, R. S., de Vernal, A., Fisher, D., Francus, P., Fréchette, B., Gajewski, K., Jennings, A., Kaufman, D. S., Miller, G., Rouston, C. and Wagner, B.: Holocene climate change in Arctic Canada and Greenland, Quat. Sci. Rev., 147, 340–364, doi:10.1016/j.quascirev.2016.02.010, 2016.

Brown, T. A., Belt, S. T., Tatarek, A. and Mundy, C. J.: Source identification of the Arctic sea ice proxy IP_{25}, Nat. Commun.,

875   5(1), 4197, doi:10.1038/ncomms5197, 2014.

Cabedo-Sanz, P., Belt, S. T., Knies, J. and Husum, K.: Identification of contrasting seasonal sea ice conditions during the Younger Dryas, Quat. Sci. Rev., 79, 74–86, doi:10.1016/j.quascirev.2012.10.028, 2013.

Cai, C., Rignot, E., Menemenlis, D. and Nakayama, Y.: Observations and modeling of ocean-induced melt beneath Petermann Glacier Ice Shelf in northwestern Greenland, Geophys. Res. Lett., 44(16), 8396–8403, doi:10.1002/2017GL073711, 2017.

880   Carr, J. R., Vieli, A., Stokes, C. R., Jamieson, S. S. R., Palmer, S. J., Christoffersen, P., Dowdeswell, J. A., Nick, F. M., Blankenship, D. D. and Young, D. A.: Basal topographic controls on rapid retreat of Humboldt Glacier, northern Greenland, J. Glaciol., 61(225), 137–150, doi:10.3189/2015JoG14J128, 2015.

Carstens, J., Hebbeln, D. and Wefer, G.: Distribution of planktic foraminifera at the ice margin in the Aictic (Fram Strait)., 1997.

885   Ceperley, E. G., Marcott, S. A., Reusche, M. M., Barth, A. M., Mix, A. C., Brook, E. J. and Caffee, M.: Widespread early Holocene deglaciation, Washington Land, northwest Greenland, Quat. Sci. Rev., 231, 106181, doi:10.1016/j.quascirev.2020.106181, 2020.

Darby, D. A., Ortiz, J. D., Grosch, C. E. and Lund, S. P.: 1,500-year cycle in the Arctic Oscillation identified in Holocene Arctic sea-ice drift, Nat. Geosci., 5(12), 897–900, doi:10.1038/ngeo1629, 2012.

890 Davidson, T. A., Wetterich, S., Johansen, K. L., Grønnow, B., Windirsch, T., Jeppesen, E., Syväranta, J., Olsen, J., González-Bergonzoni, I., Strunk, A., Larsen, N. K., Meyer, H., Søndergaard, J., Dietz, R., Eulears, I. and Mosbech, A.: The history of seabird colonies and the North Water ecosystem: Contributions from palaeoecological and archaeological evidence, Ambio, 47(2), 175–192, doi:10.1007/s13280-018-1031-1, 2018.

Dawes, P., Frisch, T., Garde, A., Iannelli, T., Ineson JR, Monrad Jensen, S., Pirajno, F., Stemmerik, L., Stouge, S. and
895 Thomassen, B.: Kane Basin 1999: mapping, stratigraphic studies and economic assessment of Precambrian and Lower Palaeozoic provinces in north-western Greenland, Geol. Greenl. Surv. Bull., 186, 11–28 [online] Available from: https://www.researchgate.net/publication/237555926 (Accessed 28 April 2020), 2000.

Dunbar, M.: The Geographical Position of the North Water on JSTOR, Arctic, 22(4), 438–441 [online] Available from: https://www.jstor.org/stable/40489906?seq=1#metadata_info_tab_contents (Accessed 27 May 2021), 1969.

900 England, J. H., Lakeman, T. R., Lemmen, D. S., Bednarski, J. M., Stewart, T. G. and Evans, D. J. A.: A millennial-scale record of Arctic Ocean sea ice variability and the demise of the Ellesmere Island ice shelves, Geophys. Res. Lett., 35(19), L19502, doi:10.1029/2008GL034470, 2008.

Fetterer, F., Knowles, K., Meier, W. N., Savoie, M. and Windnagel, A. K.: Sea Ice Index, Version 3.0, , (updated daily), doi:https://doi.org/10.7265/N5K072F8, 2017.

905 Fischer, N. and Jungclaus, J. H.: Evolution of the seasonal temperature cycle in a transient Holocene simulation: Orbital forcing and sea-ice, Clim. Past, 7(4), 1139–1148, doi:10.5194/cp-7-1139-2011, 2011.

Funder, S., Goosse, H., Jepsen, H., Kaas, E., Kjær, K. H., Korsgaard, N. J., Larsen, N. K., Linderson, H., Lyså, A., Möller, P., Olsen, J. and Willerslev, E.: A 10,000-year record of Arctic Ocean Sea-ice variability - View from the beach, Science (80-.)., 333(6043), 747–750, doi:10.1126/science.1202760, 2011.

910 Fürst, J. J., Goelzer, H. and Huybrechts, P.: Ice-dynamic projections of the Greenland ice sheet in response to atmospheric and oceanic warming, Cryosph., 9(3), 1039–1062, doi:10.5194/tc-9-1039-2015, 2015.

Gajewski, K.: Impact of Holocene climate variability on Arctic vegetation, Glob. Planet. Change, 133, 272–287, doi:10.1016/j.gloplacha.2015.09.006, 2015.

Georgiadis, E., Giraudeau, J., Jennings, A., Limoges, A., Jackson, R., Ribeiro, S. and Massé, G.: Local and regional controls
915 on Holocene sea ice dynamics and oceanography in Nares Strait, Northwest Greenland, Mar. Geol., 422, 106115, doi:10.1016/j.margeo.2020.106115, 2020.

Hansen, K. E., Giraudeau, J., Wacker, L., Pearce, C. and Seidenkrantz, M.-S.: Reconstruction of Holocene oceanographic conditions in the Northeastern Baffin Bay, Clim. Past Discuss., 1–34, doi:10.5194/cp-2019-152, 2020.

Harrison, J. C., St-Onge, M. R., Petrov, O. V, Strelnikov, S. I., Lopatin, B. G., Wilson, F. H., Tella, S., Paul, D., Lynds, T.,
920 Shokalsky, S. P., Hults, C. K., Bergman, S., Jepsen, H. F. and Solli, A.: Geological map of the Arctic., 2011.

Heuzé, C., Wåhlin, A., Johnson, H. L. and Münchow, A.: Pathways of Meltwater Export from Petermann Glacier, Greenland,

J. Phys. Oceanogr., 47(2), 405–418, doi:10.1175/jpo-d-16-0161.1, 2017.

Hill, E. A., Carr, J. R. and Stokes, C. R.: A Review of Recent Changes in Major Marine-Terminating Outlet Glaciers in Northern Greenland, Front. Earth Sci., 4, 111, doi:10.3389/feart.2016.00111, 2017.

925 Hörner, T., Stein, R., Fahl, K. and Birgel, D.: Post-glacial variability of sea ice cover, river run-off and biological production in the western Laptev Sea (Arctic Ocean) – A high-resolution biomarker study, Quat. Sci. Rev., 143, 133–149, doi:10.1016/J.QUASCIREV.2016.04.011, 2016.

Jackson, R., Kvorning, A. B., Limoges, A., Georgiadis, E., Olsen, S. M., Tallberg, P., Andersen, T. J., Mikkelsen, N., Giraudeau, J., Massé, G., Wacker, L. and Ribeiro, S.: Holocene polynya dynamics and their interaction with oceanic heat 930 transport in northernmost Baffin Bay, Sci. Rep., 11(1), 10095, doi:10.1038/s41598-021-88517-9, 2021.

Jakobsson, M., Hogan, K. A., Mayer, L. A., Mix, A., Jennings, A., Stoner, J., Eriksson, B., Jerram, K., Mohammad, R., Pearce, C., Reilly, B. and Stranne, C.: The Holocene retreat dynamics and stability of Petermann Glacier in northwest Greenland, Nat. Commun., 9(1), 2104, doi:10.1038/s41467-018-04573-2, 2018.

Jennings, A., Andrews, J. and Wilson, L.: Holocene environmental evolution of the SE Greenland Shelf North and South of 935 the Denmark Strait: Irminger and East Greenland current interactions, Quat. Sci. Rev., 30(7–8), 980–998, doi:10.1016/j.quascirev.2011.01.016, 2011a.

Jennings, A., Sheldon, C., Cronin, T., Francus, P., Stoner, J. and Andrews, J.: The Holocene History of Nares Strait: Transition from Glacial Bay to Arctic-Atlantic Throughflow, Oceanography, 24(3), 26–41, doi:10.5670/oceanog.2011.52, 2011b.

Jennings, A., Andrews, J., Reilly, B., Walczak, M., Jakobsson, M., Mix, A., Stoner, J., Nicholls, K. W. and Cheseby, M.: 940 Modern foraminiferal assemblages in northern Nares Strait, Petermann Fjord, and beneath Petermann ice tongue, NW Greenland, Arctic, Antarct. Alp. Res., 52(1), 491–511, doi:10.1080/15230430.2020.1806986, 2020.

Johannessen, O. M., Babiker, M. and Miles, M. W.: Unprecedented Retreat in a 50-Year Observational Record for Petermann Glacier, North Greenland, Atmos. Ocean. Sci. Lett., 6(5), 259–265, doi:10.3878/j.issn1674-2834.13.0021, 2013.

Johnson, H. L., Münchow, A., Falkner, K. K. and Melling, H.: Ocean circulation and properties in Petermann Fjord, Greenland, 945 J. Geophys. Res., 116(C1), C01003, doi:10.1029/2010JC006519, 2011.

Jones, P. E. and Eert, J. A.: Waters of Nares Strait in 2001, Polarforschung, 74(1–3), 185–189 [online] Available from: https://www.researchgate.net/publication/237280056_Waters_of_Nares_Strait_in_2001 (Accessed 12 February 2020), 2004.

Kaufman, D. ., Ager, T. ., Anderson, N. ., Anderson, P. ., Andrews, J. ., Bartlein, P. ., Brubaker, L. ., Coats, L. ., Cwynar, L. ., Duvall, M. ., Dyke, A. ., Edwards, M. ., Eisner, W. ., Gajewski, K., Geirsdóttir, A., Hu, F. ., Jennings, A. ., Kaplan, M. ., 950 Kerwin, M. ., Lozhkin, A. ., MacDonald, G. ., Miller, G. ., Mock, C. ., Oswald, W. ., Otto-Bliesner, B. ., Porinchu, D. ., Rühland, K., Smol, J. ., Steig, E. . and Wolfe, B. .: Holocene thermal maximum in the western Arctic (0–180°W), Quat. Sci. Rev., 23(5–6), 529–560, doi:10.1016/J.QUASCIREV.2003.09.007, 2004.

Knudsen, K. L., Stabell, B., Seidenkrantz, M.-S., Eiriksson, J. and Blake, W.: Deglacial and Holocene conditions in northernmost Baffin Bay: sediments, foraminifera, diatoms and stable isotopes, Boreas, 37(3), 346–376, doi:10.1111/j.1502- 955 3885.2008.00035.x, 2008.

Kwok, R.: Variability of Nares Strait ice flux, Geophys. Res. Lett., 32(24), L24502, doi:10.1029/2005GL024768, 2005.

Kwok, R., Toudal Pedersen, L., Gudmandsen, P. and Pang, S. S.: Large sea ice outflow into the Nares Strait in 2007, Geophys. Res. Lett., 37(3), L03502, doi:10.1029/2009GL041872, 2010.

Lasher, G. E., Axford, Y., McFarlin, J. M., Kelly, M. A., Osterberg, E. C. and Berkelhammer, M. B.: Holocene temperatures and isotopes of precipitation in Northwest Greenland recorded in lacustrine organic materials, Quat. Sci. Rev., 170, 45–55, doi:10.1016/j.quascirev.2017.06.016, 2017.

Lecavalier, B. S., Fisher, D. A., Milne, G. A., Vinther, B. M., Tarasov, L., Huybrechts, P., Lacelle, D., Main, B., Zheng, J., Bourgeois, J. and Dyke, A. S.: High Arctic Holocene temperature record from the Agassiz ice cap and Greenland ice sheet evolution, Proc. Natl. Acad. Sci. U. S. A., 114(23), 5952–5957, doi:10.1073/pnas.1616287114, 2017.

Ledu, D., Rochon, A., de Vernal, A. and St-Onge, G.: Holocene paleoceanography of the northwest passage, Canadian Arctic Archipelago, Quat. Sci. Rev., 29(25–26), 3468–3488, doi:10.1016/J.QUASCIREV.2010.06.018, 2010.

Leu, E., Mundy, C. J., Assmy, P., Campbell, K., Gabrielsen, T. M., Gosselin, M., Juul-Pedersen, T. and Gradinger, R.: Arctic spring awakening - Steering principles behind the phenology of vernal ice algal blooms, Prog. Oceanogr., 139, 151–170, doi:10.1016/j.pocean.2015.07.012, 2015.

Limoges, A., Weckström, K., Ribeiro, S., Georgiadis, E., Hansen, K. E., Martinez, P., Seidenkrantz, M., Giraudeau, J., Crosta, X. and Massé, G.: Learning from the past: impact of the Arctic Oscillation on sea ice and marine productivity off northwest Greenland over the last 9000 years, Glob. Chang. Biol., gcb.15334, doi:10.1111/gcb.15334, 2020.

Lougheed, B. C. and Obrochta, S. P.: MatCal: Open Source Bayesian 14C Age Calibration in Matlab, J. Open Res. Softw., 4(1), doi:10.5334/jors.130, 2016.

Marcott, S. A., Shakun, J. D., Clark, P. U. and Mix, A. C.: A reconstruction of regional and global temperature for the past 11,300 years, Science (80-.)., 339(6124), 1198–1201, doi:10.1126/science.1228026, 2013.

Matsuo, A. and Sato, A.: Sterols of mosses, Phytochemistry, 30(7), 2305–2306, doi:10.1016/0031-9422(91)83635-X, 1991.

Mayot, N., Matrai, P. A., Arjona, A., Bélanger, S., Marchese, C., Jaegler, T., Ardyna, M. and Steele, M.: Springtime Export of Arctic Sea Ice Influences Phytoplankton Production in the Greenland Sea, J. Geophys. Res. Ocean., 125(3), doi:10.1029/2019JC015799, 2020.

Melling, H., Gratton, Y. and Ingram, G.: Ocean circulation within the North Water polynya of Baffin Bay, Atmosphere-Ocean, 39(3), 301–325, doi:10.1080/07055900.2001.9649683, 2001.

Meyers, P. A. and Ishiwatari, R.: Lacustrine organic geochemistry-an overview of indicators of organic matter sources and diagenesis in lake sediments, Org. Geochem., 20(7), 867–900, doi:10.1016/0146-6380(93)90100-P, 1993.

Mode, W. N.: The Terrestrial Record of Postglacial Vegetation and Climate from the Arctic/Subarctic of Eastern Canada and West Greenland, Geosci. Canada, 23(4), 1996.

Möller, P., Larsen, N. K., Kjær, K. H., Funder, S., Schomacker, A., Linge, H. and Fabel, D.: Early to middle Holocene valley glaciations on northernmost Greenland, Quat. Sci. Rev., 29(25–26), 3379–3398, doi:10.1016/j.quascirev.2010.06.044, 2010.

Moore, G. W. K., Howell, S. E. L., Brady, M., Xu, X. and McNeil, K.: Anomalous collapses of Nares Strait ice arches leads

990   to enhanced export of Arctic sea ice, Nat. Commun., 12(1), 1–8, doi:10.1038/s41467-020-20314-w, 2021.

Münchow, A.: Volume and Freshwater Flux Observations from Nares Strait to the West of Greenland at Daily Time Scales from 2003 to 2009, J. Phys. Oceanogr., 46(1), 141–157, doi:10.1175/JPO-D-15-0093.1, 2016.

Münchow, A. and Melling, H.: Ocean current observations from Nares Strait to the west of Greenland: Interannual to tidal variability and forcing, J. Mar. Res., 66(6), 801–833, doi:10.1357/002224008788064612, 2008.

995   Münchow, A., Falkner, K. K. and Melling, H.: Spatial continuity of measured seawater and tracer fluxes through Nares Strait, a dynamically wide channel bordering the Canadian Archipelago, J. Mar. Res., 65(6), 759–788, doi:10.1357/002224007784219048, 2007.

Münchow, A., Falkner, K., Melling, H., Rabe, B. and Johnson, H.: Ocean Warming of Nares Strait Bottom Waters off Northwest Greenland, 2003–2009, Oceanography, 24(3), 114–123, doi:10.5670/oceanog.2011.62, 2011a.

1000 Münchow, A., Falkner, K., Melling, H., Rabe, B. and Johnson, H.: Ocean Warming of Nares Strait Bottom Waters off Northwest Greenland, 2003–2009, Oceanography, 24(3), 114–123, doi:10.5670/oceanog.2011.62, 2011b.

Münchow, A., Padman, L. and Fricker, H. A.: Interannual changes of the floating ice shelf of Petermann Gletscher, North Greenland, from 2000 to 2012, J. Glaciol., 60(221), 489–499, doi:10.3189/2014JoG13J135, 2014.

Nagler, T., Rott, H., Hetzenecker, M., Wuite, J. and Potin, P.: The Sentinel-1 Mission: New Opportunities for Ice Sheet
1005 Observations, Remote Sens., 7(7), 9371–9389, doi:10.3390/rs70709371, 2015.

Navarro-Rodriguez, A., Belt, S. T., Knies, J. and Brown, T. A.: Mapping recent sea ice conditions in the Barents Sea using the proxy biomarker IP25: implications for palaeo sea ice reconstructions, Quat. Sci. Rev., 79, 26–39, doi:10.1016/J.QUASCIREV.2012.11.025, 2013.

Pados, T. and Spielhagen, R. F.: Species distribution and depth habitat of recent planktic foraminifera in Fram Strait, Arctic
1010 Ocean, Polar Res., 33(1 SUPPL), doi:10.3402/polar.v33.22483, 2014.

Parnell, J., Bowden, S., Andrews, J. T. and Taylor, C.: Biomarker determination as a provenance tool for detrital carbonate events (Heinrich events?): Fingerprinting Quaternary glacial sources into Baffin Bay, Earth Planet. Sci. Lett., 257(1–2), 71–82, doi:10.1016/j.epsl.2007.02.021, 2007.

Rabe, B., Münchow, A., Johnson, H. L. and Melling, H.: Nares Strait hydrography and salinity field from a 3-year moored
1015 array, J. Geophys. Res., 115(C7), C07010, doi:10.1029/2009JC005966, 2010.

Rabe, B., Johnson, H. L., Münchow, A. and Melling, H.: Geostrophic ocean currents and freshwater fluxes across the Canadian polar shelf via Nares Strait, J. Mar. Res., 70(4), 603–640, doi:10.1357/002224012805262725, 2012.

Rasmussen, T. A. S., Kliem, N. and Kaas, E.: Modelling the sea ice in the Nares Strait, Ocean Model., 35(3), 161–172, doi:10.1016/j.ocemod.2010.07.003, 2010.

1020 Reilly, B. T., Stoner, J. S., Mix, A. C., Walczak, M. H., Jennings, A., Jakobsson, M., Dyke, L., Glueder, A., Nicholls, K., Hogan, K. A., Mayer, L. A., Hatfield, R. G., Albert, S., Marcott, S., Fallon, S. and Cheseby, M.: Holocene break-up and reestablishment of the Petermann Ice Tongue, Northwest Greenland, Quat. Sci. Rev., 218, 322–342, doi:10.1016/j.quascirev.2019.06.023, 2019.

Reimer, P. J., Bard, E., Bayliss, A., Beck, J. W., Blackwell, P. G., Ramsey, C. B., Buck, C. E., Cheng, H., Edwards, R. L.,
1025 Friedrich, M., Grootes, P. M., Guilderson, T. P., Haflidason, H., Hajdas, I., Hatté, C., Heaton, T. J., Hoffmann, D. L., Hogg,
A. G., Hughen, K. A., Kaiser, K. F., Kromer, B., Manning, S. W., Niu, M., Reimer, R. W., Richards, D. A., Scott, E. M.,
Southon, J. R., Staff, R. A., Turney, C. S. M. and van der Plicht, J.: IntCal13 and Marine13 Radiocarbon Age Calibration
Curves 0–50,000 Years cal BP, Radiocarbon, 55(4), 1869–1887, doi:10.2458/azu_js_rc.55.16947, 2013.

Ribeiro, S., Sejr, M. K., Limoges, A., Heikkilä, M., Andersen, T. J., Tallberg, P., Weckström, K., Husum, K., Forwick, M.,
1030 Dalsgaard, T., Massé, G., Seidenkrantz, M.-S. and Rysgaard, S.: Sea ice and primary production proxies in surface sediments
from a High Arctic Greenland fjord: Spatial distribution and implications for palaeoenvironmental studies, Ambio, 46(S1),
106–118, doi:10.1007/s13280-016-0894-2, 2017.

Rignot, E. and Kanagaratnam, P.: Changes in the Velocity Structure of the Greenland Ice Sheet, Science (80-.)., 311(5763),
986–990, doi:10.1126/science.1121381, 2006.

1035 Rignot, E. and Steffen, K.: Channelized bottom melting and stability of floating ice shelves, Geophys. Res. Lett., 35(2),
L02503, doi:10.1029/2007GL031765, 2008.

Robel, A. A.: Thinning sea ice weakens buttressing force of iceberg mélange and promotes calving, Nat. Commun., 8, 14596,
doi:10.1038/ncomms14596, 2017.

Rontani, J. F., Charrière, B., Sempéré, R., Doxaran, D., Vaultier, F., Vonk, J. E. and Volkman, J. K.: Degradation of sterols
1040 and terrigenous organic matter in waters of the Mackenzie Shelf, Canadian Arctic, Org. Geochem., 75, 61–73,
doi:10.1016/j.orggeochem.2014.06.002, 2014.

Rückamp, M., Neckel, N., Berger, S., Humbert, A. and Helm, V.: Calving Induced Speedup of Petermann Glacier, J. Geophys.
Res. Earth Surf., 124(1), 216–228, doi:10.1029/2018JF004775, 2019.

Ruttenberg, K. C. and Goñi, M. A.: Phosphorus distribution, C:N:P ratios, and δ13C(OC) in arctic, temperate, and tropical
1045 coastal sediments: Tools for characterizing bulk sedimentary organic matter, Mar. Geol., 139(1–4), 123–145,
doi:10.1016/S0025-3227(96)00107-7, 1997.

Ryan, P. A. and Münchow, A.: Sea ice draft observations in Nares Strait from 2003 to 2012, J. Geophys. Res. Ocean., 122(4),
3057–3080, doi:10.1002/2016JC011966, 2017.

Safe, S., Safe, L. M. and Maass, W. S. G.: Sterols of three lichen species: Lobaria pulmonaria, Lobaria Scrobiculata and Usnea
1050 Longissima, Phytochemistry, 14(8), 1821–1823, doi:10.1016/0031-9422(75)85302-7, 1975.

Samelson, R. M., Agnew, T., Melling, H. and Münchow, A.: Evidence for atmospheric control of sea-ice motion through
Nares Strait, Geophys. Res. Lett., 33(2), L02506, doi:10.1029/2005GL025016, 2006.

Seidenkrantz, M. S.: Benthic foraminifera as palaeo sea-ice indicators in the subarctic realm - examples from the Labrador
Sea-Baffin Bay region, Quat. Sci. Rev., 79, 135–144, doi:10.1016/j.quascirev.2013.03.014, 2013.

1055 Shepherd, A., Ivins, E. R., Geruo, A., Barletta, V. R., Bentley, M. J., Bettadpur, S., Briggs, K. H., Bromwich, D. H., Forsberg,
R., Galin, N., Horwath, M., Jacobs, S., Joughin, I., King, M. A., Lenaerts, J. T. M., Li, J., Ligtenberg, S. R. M., Luckman, A.,
Luthcke, S. B., McMillan, M., Meister, R., Milne, G., Mouginot, J., Muir, A., Nicolas, J. P., Paden, J., Payne, A. J., Pritchard,

H., Rignot, E., Rott, H., Sørensen, L. S., Scambos, T. A., Scheuchl, B., Schrama, E. J. O., Smith, B., Sundal, A. V., Van Angelen, J. H., Van De Berg, W. J., Van Den Broeke, M. R., Vaughan, D. G., Velicogna, I., Wahr, J., Whitehouse, P. L., Wingham, D. J., Yi, D., Young, D. and Zwally, H. J.: A reconciled estimate of ice-sheet mass balance, Science (80-.)., 338(6111), 1183–1189, doi:10.1126/science.1228102, 2012.

Shroyer, E. L., Samelson, R. M., Padman, L. and Münchow, A.: Modeled ocean circulation in Nares Strait and its dependence on landfast-ice cover, J. Geophys. Res. Ocean., 120(12), 7934–7959, doi:10.1002/2015JC011091, 2015.

Shroyer, E. L., Padman, L., Samelson, R. M., Münchow, A. and Stearns, L. A.: Seasonal control of Petermann Gletscher ice-shelf melt by the ocean's response to sea-ice cover in Nares Strait, J. Glaciol., 63(238), 324–330, doi:10.1017/jog.2016.140, 2017.

Smik, L., Cabedo-Sanz, P. and Belt, S. T.: Semi-quantitative estimates of paleo Arctic sea ice concentration based on source-specific highly branched isoprenoid alkenes: A further development of the PIP25 index, Org. Geochem., 92, 63–69, doi:10.1016/J.ORGGEOCHEM.2015.12.007, 2016.

Stein, R., Fahl, K., Schade, I., Manerung, A., Wassmuth, S., Niessen, F. and Nam, S.-I.: Holocene variability in sea ice cover, primary production, and Pacific-Water inflow and climate change in the Chukchi and East Siberian Seas (Arctic Ocean), J. Quat. Sci., 32(3), 362–379, doi:10.1002/jqs.2929, 2017.

Stocker, T. F., Qin, D., Plattner, G.-K., Tignor, M. M. B., Allen, S. K., Boschung, J., Nauels, A., Xia, Y., Bex, V. and Midgley, P. M.: Climate Change 2013 The Physical Science Basis Working Group I Contribution to the Fifth Assessment Report of the Intergovernmental Panel on Climate Change Edited by. [online] Available from: www.cambridge.org (Accessed 1 May 2020), 2013.

Tinto, K. J., BellTinto, K.J., Bell, R.E., Cochran, J.R., Münchow, A., 2015. Bathymetry in Petermann fjord from Operation IceBridge aerogravity. Earth Planet. Sci. Lett. 422, 58–66. https://doi.org/10.1016/j.epsl.2015.04.009, R. E., Cochran, J. R. and Münchow, A.: Bathymetry in Petermann fjord from Operation IceBridge aerogravity, Earth Planet. Sci. Lett., 422, 58–66, doi:10.1016/j.epsl.2015.04.009, 2015.

Todd, J. and Christoffersen, P.: Are seasonal calving dynamics forced by buttressing from ice mélange or undercutting by melting? Outcomes from full-Stokes simulations of Store Glacier, West Greenland, Cryosph., 8(6), 2353–2365, doi:10.5194/tc-8-2353-2014, 2014.

Vare, L. L., Massé, G., Gregory, T. R., Smart, C. W. and Belt, S. T.: Sea ice variations in the central Canadian Arctic Archipelago during the Holocene, Quat. Sci. Rev., 28(13–14), 1354–1366, doi:10.1016/j.quascirev.2009.01.013, 2009.

Vincent, R. F.: A Study of the North Water Polynya Ice Arch using Four Decades of Satellite Data, Sci. Rep., 9(1), 1–12, doi:10.1038/s41598-019-56780-6, 2019.

Vinther, B. M., Buchardt, S. L., Clausen, H. B., Dahl-Jensen, D., Johnsen, S. J., Fisher, D. A., Koerner, R. M., Raynaud, D., Lipenkov, V., Andersen, K. K., Blunier, T., Rasmussen, S. O., Steffensen, J. P. and Svensson, A. M.: Holocene thinning of the Greenland ice sheet, Nature, 461(7262), 385–388, doi:10.1038/nature08355, 2009.

Volkman, J. K.: A review of sterol markers for marine and terrigenous organic matter, Org. Geochem., 9(2), 83–99,

doi:10.1016/0146-6380(86)90089-6, 1986.

Volkman, J. K.: Sterols in microorganisms, Appl Microbiol Biotechnol, 60, 495–506, doi:10.1007/s00253-002-1172-8, 2003.

Volkman, J. K., Barrett, S. M., Dunstan, G. A. and Jeffrey, S. W.: Geochemical significance of the occurrence of dinosterol and other 4-methyl sterols in a marine diatom, Org. Geochem., 20(1), 7–15, doi:10.1016/0146-6380(93)90076-N, 1993.

Volkman, J. K., Rohjans, D., Rullkötter, J., Scholz-Böttcher, B. M. and Liebezeit, G.: Sources and diagenesis of organic matter in tidal flat sediments from the German Wadden Sea, Cont. Shelf Res., 20(10–11), 1139–1158, doi:10.1016/S0278-4343(00)00016-9, 2000.

Washam, P., Münchow, A. and Nicholls, K. W.: A Decade of Ocean Changes Impacting the Ice Shelf of Petermann Gletscher, Greenland, J. Phys. Oceanogr., 48(10), 2477–2493, doi:10.1175/JPO-D-17-0181.1, 2018.

Washam, P., Nicholls, K. W., Münchow, A. and Padman, L.: Summer surface melt thins Petermann Gletscher Ice Shelf by enhancing channelized basal melt, J. Glaciol., 65(252), 662–674, doi:10.1017/jog.2019.43, 2019.

Wassmann, P. and Reigstad, M.: Future Arctic Ocean seasonal ice zones and implications for pelagic-benthic coupling, Oceanography, 24(3), 220–231, doi:10.5670/oceanog.2011.74, 2011.

Xiao, X., Fahl, K. and Stein, R.: Biomarker distributions in surface sediments from the Kara and Laptev seas (Arctic Ocean): indicators for organic-carbon sources and sea-ice coverage, Quat. Sci. Rev., 79, 40–52, doi:10.1016/J.QUASCIREV.2012.11.028, 2013.

Xiao, X., Fahl, K., Müller, J. and Stein, R.: Sea-ice distribution in the modern Arctic Ocean: Biomarker records from trans-Arctic Ocean surface sediments, Geochim. Cosmochim. Acta, 155, 16–29, doi:10.1016/J.GCA.2015.01.029, 2015.

Yunker, M. B., Macdonald, R. W., Veltkamp, D. J. and Cretney, W. J.: Terrestrial and marine biomarkers in a seasonally ice-covered Arctic estuary - integration of multivariate and biomarker approaches, Mar. Chem., 49(1), 1–50, doi:10.1016/0304-4203(94)00057-K, 1995.